

# Anyonic statistics and slow quasiparticle dynamics in a graphene fractional quantum Hall interferometer

Noah L. Samuelson,<sup>1,\*</sup> Liam A. Cohen,<sup>1,\*</sup> Will Wang,<sup>1</sup> Simon Blanch,<sup>1</sup> Takashi Taniguchi,<sup>2</sup> Kenji Watanabe,<sup>3</sup> Michael P. Zaletel,<sup>4,5</sup> and Andrea F. Young<sup>1,†</sup>

<sup>1</sup>*Department of Physics, University of California at Santa Barbara, Santa Barbara CA 93106, USA*

<sup>2</sup>*International Center for Materials Nanoarchitectonics,*

*National Institute for Materials Science, 1-1 Namiki, Tsukuba 305-0044, Japan*

<sup>3</sup>*Research Center for Functional Materials, National Institute for Materials Science, 1-1 Namiki, Tsukuba 305-0044, Japan*

<sup>4</sup>*Department of Physics, University of California, Berkeley, California 94720, USA*

<sup>5</sup>*Material Science Division, Lawrence Berkeley National Laboratory, Berkeley, California 94720, USA*

(Dated: May 30, 2024)

Anyons are two dimensional particles with fractional exchange statistics that emerge as elementary excitations of fractional quantum Hall phases[1–5]. Experimentally, anyonic statistics manifest directly in the edge-state Fabry-Pérot interferometer geometry[6–9], where the presence of  $N_{qp}$  localized anyons in the interferometer bulk contributes a phase  $N_{qp}\theta_a$  to the observed interference pattern, where  $\theta_a$  is twice the statistical exchange phase[10]. Here, we report a measurement of  $\theta_a$  in a monolayer graphene Fabry-Pérot interferometer at  $\nu = 1/3$ . We find a preponderance of phase slips with magnitudes  $\Delta\theta \approx 2\pi/3$ , confirming the result of past experiments in GaAs quantum wells[11, 12] and consistent with expectations for the tunneling of Abelian anyons into the interferometer bulk. In contrast to prior work, however, single anyon tunneling events manifest as instantaneous and irreversible phase slips, indicative of quasiparticle equilibration times exceeding 20 minutes in some cases. We use the discrepancy between the quasiparticle equilibration rate and our measurement speed to vary the interferometer area  $A_I$  and  $N_{qp}$  independently, allowing us to precisely determine the interferometer phase and monitor the entry and exit of individual anyons to the interferometer loop in the time domain. Besides providing a replication of previous interferometric measurements sensitive to  $\theta_a$  in GaAs [11], our results bring anyon dynamics into the experimental regime and suggest that the average ‘topological charge’ of a mesoscopic quantum Hall device can be held constant over hour long timescales.

## INTRODUCTION

When an Abelian anyon is brought along a closed trajectory encircling  $N_{qp}$  localized anyons, its wavefunction accumulates a phase

$$\frac{\theta}{2\pi} = \frac{e^* A_I B}{e \Phi_0} + N_{qp} \frac{\theta_a}{2\pi}, \quad (1)$$

where  $A_I$  is the area of the loop,  $B$  is the applied magnetic field,  $\theta_a$  is twice the exchange phase, and  $e^*$  is the quasiparticle charge. Quantum Hall edge state Fabry-Pérot interferometers exploit the contrast between localized anyons in the bulk and propagating anyonic quasiparticles along the chiral edge modes to directly observe this phase[6–9]. In a Fabry-Pérot interferometer, delocalized quasiparticles enter the cavity via a quantum point contact (QPC) and propagate along the edge to a second QPC; they can then exit the cavity immediately or complete an integer number of additional circuits before exiting. Trajectories differing by the number of circuits give an interference contribution to the conductance,  $\delta G$ , that is periodic in  $\theta$  and can be measured as a function of  $B$ ,  $A_I$ , or  $N_{qp}$ . The clearest signature of anyonic statistics is expected if  $N_{qp}$  changes discretely while keeping  $A_I$  and  $B$  fixed; the resulting jump in  $\theta$  then gives  $\theta_a$  directly.

Fabry-Pérot interferometers have been investigated in GaAs heterostructures for nearly two decades[11–21]. These experiments have revealed that Coulomb interactions may prevent observation of the anyon phase[9]. Specifically, as charge enters the bulk of the interferometer, Coulomb repul-

sion may cause a change in  $A_I$ , leading to an observable phase shift even for fermionic quasiparticles. If the ‘‘bulk-edge coupling’’ is large, this change in the Aharonov-Bohm phase can completely obscure the contribution of  $\theta_a$ . Recently, a breakthrough in the design of GaAs heterostructures led to the observation of phase shifts that agree quantitatively with the expected  $\theta_a = 2\pi/3$  in the  $\nu = 1/3$  state[11, 12, 20, 22]. Graphene heterostructures are a natural venue in which to extend these results owing to the large fractional quantum Hall energy gaps observed at both odd-[23–26] and even-denominator filling factors[27–31]. Moreover, the nearby graphite gates in typical dual-gated geometries ensure a high degree of screening, suppressing bulk-edge coupling. Indeed, measurements of Fabry-Pérot interferometers in graphene have uniformly observed Aharonov-Bohm dominated interference[32–36]; however, no measurements of the anyon phase at fractional filling have been reported.

## FABRY-PÉROT INTERFERENCE IN $\nu = 1/3$

In this work, we study a monolayer graphene gate-defined Fabry-Pérot interferometer, shown schematically in Fig. 1a. The interferometer is fabricated using anodic-oxidation lithography to define the gate structure in a graphite layer, which is then combined using dry van der Waals assembly techniques to form a device with six separately-gated regions[37]. In our device (Fig. 1a), two pairs of gates (NE/SE and NW/SW) define QPCs, while a plunger gate (P) provides

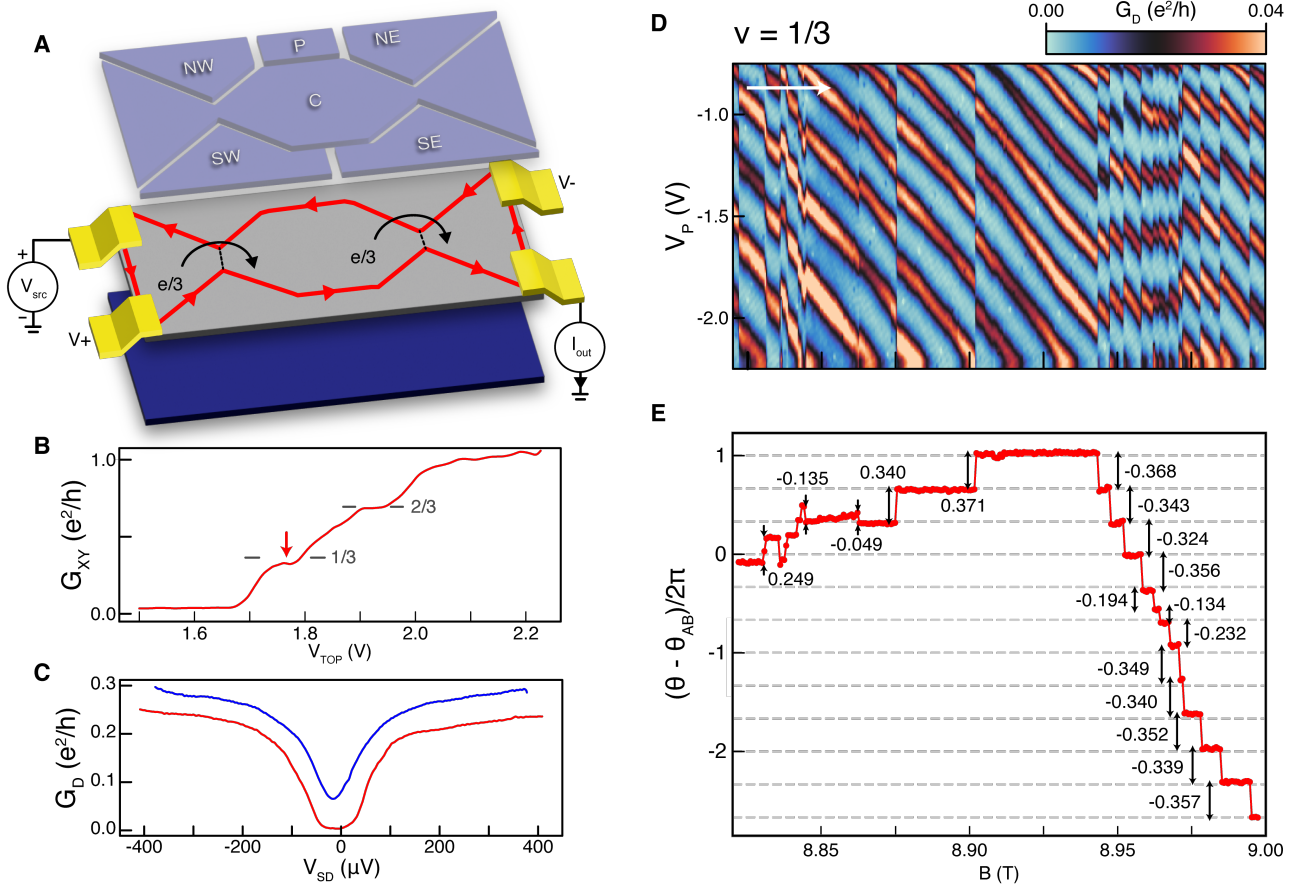


FIG. 1. **Fabry-Pérot interference in the  $\nu = 1/3$  state** (A) Schematic of the dual-graphite gated edge state Fabry-Pérot interferometer. The gates defining the interferometer are labeled C, NW, SW, NE, SE and P. Edge states are formed in the monolayer graphene around the center-gated region (C) and enter the interferometer via two QPCs tuned by the NW/SW and NE/SE gates. There is also a global graphite back gate. (B) Hall conductance  $G_{XY}$  measured on the west side of the device as a function of the voltage  $V_{TOP}$  applied to all top gates together, with a fixed back gate voltage  $V_{BG} = -1.5$  V. (C) Conductance through each QPC vs. the DC source-drain bias  $V_{SD}$  (applied as an added voltage on the source electrode), with the C region fixed at the density corresponding to the marked point in the  $1/3$  plateau in panel B. The blue trace was taken with the NW/SW regions at filling  $1/3$ , and the NE/SE regions depleted. The red trace was taken with the NE/SE regions at filling  $1/3$  and the NW/SW regions depleted (see Supplement for the individual QPC pinch-off curves). (D)  $G_D$  measured across the interferometer at  $\nu = 1/3$ , with both QPCs partially transmitting. The magnetic field is swept from low to high. (E) The phase extracted from the Fourier transform of the data in panel D. A continuous Aharonov-Bohm phase is subtracted, and we adopt the convention  $\Delta\theta \in (-\pi, \pi)$ .

additional control of the interferometer area. The center gate (C) and a global graphite bottom gate are used, together, to set the filling factor and, through fringe electric fields, adjust the transmission through the QPCs. Transport data at  $B = 9$  T as a function of a common voltage applied to all six top gates in Fig. 1b show well-developed plateaus at filling factor  $1/3$  and  $2/3$ . We operate our interferometer within the  $1/3$  plateau at the indicated point at  $B = 9$  T. We measure the transmission through the interferometer via the diagonal conductance,  $G_D \equiv I_{out}/(V_+ - V_-)$  (see Fig. 1a). To confirm that our experiment is probing chiral edge modes of the  $1/3$  state, we measure the source-drain bias dependence of the two QPCs in the partial transmission regime individually. As shown in Fig. 1c, both show strong suppression of  $G_D$  at low bias, as expected for tunneling between chiral Luttinger liquids at the QPCs[38–45]. This behavior is neither expected

nor observed in the integer quantum Hall regime (see Supplement for a comparable measurement in the  $\nu = 2$  state, showing no zero-bias suppression).

Fig. 1d shows  $G_D$  at  $\nu = 1/3$  with both QPCs set to partial pinch-off as a function of  $V_P$  and  $B$ . The interference shows high-visibility oscillations with lines of constant phase having a negative slope in the  $V_P - B$  plane, consistent with an Aharonov-Bohm dominated interference phase[9]. Following Eq. (1), we estimate the effective interferometer area to be  $A_I = 3\Phi_0/\Delta B = 0.69 - 0.83\mu m^2$  based on the  $\Delta B \approx 15 - 18$  mT field period of the oscillations. This agrees with the nominal device area of  $0.74 - 0.83\mu m^2$  of the patterned graphite gates, without accounting for bulk-edge coupling, suggesting such coupling is small (see supplement) [9].

The edge velocity may be estimated from the period of the interference as a function of a common-mode DC volt-

age applied to the transport leads, shown in the supplement. [7, 16, 46]. This gives an edge state capacitance  $C_I = e/\Delta V_{\text{CM}} = e^2/234 \mu\text{eV}$  from which the edge velocity follows via the relation  $\frac{\hbar v}{\nu L} = 234 \mu\text{eV}$ . Taking  $L = 3.30(11) \mu\text{m}$  we obtain  $v = 6.2 \pm 0.2 \times 10^4 \text{m/s}$ , comparable to prior estimates for the velocity of integer quantum Hall edge states in graphene systems[32, 33, 35, 47] but several times larger than measured in GaAs quantum wells under similar external conditions[11].

In addition to the continuously-tuned Aharonov-Bohm phase giving rise to the negative slope, the oscillations in Fig. 1d are punctuated by sharp ‘slips’ where the interference phase changes suddenly between  $V_P$  traces taken at consecutive values of  $B$ . The majority of the events are effectively instantaneous with respect to the 30-second measurement time of each individual  $V_P$  trace, manifesting as a discontinuity between traces taken at subsequent magnetic fields. To quantify the magnitude of the phase slips, we compute the Fourier transform of  $G_D$  with respect to  $V_P$  for each value of  $B$  and extract the phase of the largest-magnitude peak, which determines the oscillation phase  $\theta$ . Per Eq. (1),  $\theta$  is expected to contain both a smoothly-varying Aharonov-Bohm contribution as well as an anyonic contribution proportional to  $N_{qp}$ . To isolate the latter, we take a running trimmed-mean of the line-by-line phase difference and subtract it from the measured phase.

The residual phase,  $\theta - \theta_{AB}$ , is plotted in Fig. 1e. We can only determine phase differences  $\text{mod } 2\pi$ , so we take the convention that the phase slips lie in the interval  $(-\pi, \pi)$ . We mark the magnitude of each phase slip calculated from the difference in average value between intervals of stable phase. The statistical error in the phase slip measurements is small; repeated measurements within a single interval of stable phase show a standard deviation of  $\sigma_\theta \approx .012$ . A larger source of error arises from the fact that the oscillations are not perfectly periodic in  $V_P$ , generating different values of  $\theta$  for different components of the Fourier transform. We estimate that this error may be as high as  $\pm 2\pi \times .04$  (see supplement). Most of the marked phase slips are consistent, within this uncertainty, with  $\theta_a = 2\pi/3$ . We interpret each event as corresponding to the entry of a single charge- $e/3$  anyon into the interferometer.

The small deviation in the phase slip magnitudes from the predicted value suggests a low degree of bulk-edge coupling for many of the events[9, 48]. To assess the plausibility of this in our geometry, we estimate the bulk-edge coupling for an anyon entering a localized impurity state a distance  $R > d$  from the edge, where  $d = 45 \text{nm}$  is the gate distance. When a charge  $e/3$  fills such a state, the compressible edge will partially screen the resulting potential, effectively increasing  $A_I$ . Accounting for the electrostatics of a double-gated device (see supplement), this edge screening will induce a charge

$$\delta Q_I \approx -\frac{e}{3} \frac{C_I}{\pi \sqrt{\epsilon_{xy} \epsilon_z} L} \exp\left(-\frac{\pi R}{2d} \sqrt{\frac{\epsilon_z}{\epsilon_{xy}}}\right), \quad (2)$$

where  $\epsilon_{xy} = 6.6$  and  $\epsilon_z = 3$  are the dielectric constants of the hexagonal boron nitride dielectric, and  $L$  is the perimeter

of the interferometer. Taking the measured values of  $C_I$  and  $L$ , the bulk-edge coupling contribution to the phase slip is  $\delta\theta = 2\pi \times \delta Q_I/e \approx 2\pi \times 0.57 e^{-R/42.5 \text{nm}}$ . For  $R > 110 \text{nm}$ , corresponding to approximately half of our interferometer area, this correction is less than our experimental uncertainty. Assuming impurity sites to be randomly distributed, then, it is reasonable that the plurality of events will have undetectable bulk-edge coupling.

However, not all of the  $\nu = 1/3$  phase slips are consistent with the quantized value, suggesting that some impurity sites do trap quasiparticles near the edge. For example, we observe several slips with  $\Delta\theta \approx \pm 2\pi \times 0.25$ . From Eq. (2), we estimate the position of the impurity trapping an anyon to be a distance  $R \approx 80 \text{nm}$  from the perimeter. Similarly, a pair of slips near  $B = 8.963 \text{T}$  show magnitudes of  $-2\pi \times .194$  and  $-2\pi \times 0.134$  whose sum,  $-2\pi \times 0.328$ , agrees with the quantized value of  $\theta_a$ . This is consistent with an anyon entering an impurity state  $R \approx 60 \text{nm}$  from the edge before moving to an impurity state with negligible bulk edge coupling shortly afterwards.

We may compare these results with previous experiments in GaAs quantum wells[11, 20]. Near the center of the fractional quantum Hall plateau, those experiments observed rare, nearly-quantized phase slips. Outside of this hard-gap region, the interference signal shows a large increase in the field period and a substantial reduction in the interference amplitude. This latter behavior was interpreted as the entry of one  $e/3$  anyon with every flux quantum, so as to keep the density constant. In this thermodynamically compressible regime, the Aharonov-Bohm and statistical phases cancel (on average), keeping  $\theta(B)$  nearly constant. However, in this regime no sharp phase slips associated with anyon entry or exit were reported, a phenomenon understood to result from rapid thermal fluctuations in the anyon number when states with  $N_{qp}$  and  $N_{qp} + 1$  are close to degeneracy. Notably, in this picture fast equilibration between the bulk anyon occupation and the gapless edge plays a key role.

As in GaAs, we observe a region of continuous, Aharonov-Bohm driven phase evolution between  $B = 8.85 \text{T}$  and  $B = 8.93 \text{T}$  interrupted by a small number of nearly-quantized phase slips. This is expected for a ‘hard’ gap with only rare impurity states available to host localized anyonic quasiparticles[11]. For  $B > 8.93 \text{T}$ , in contrast, we observe a cascade of events, where a phase slip occurs on average once per flux quantum, as expected outside the hard gap where the system is thermodynamically compressible. However, we observe no diminution of the interference amplitude in this regime: each slip remains sharp and close to the quantized value despite the average value of  $\theta(B)$  remaining constant. Moreover, none of the phase slips shown in Fig. 1d show an experimentally resolvable slope in the  $V_P - B$  plane. These findings contrast with experiments on GaAs, where both  $V_P$  and  $B$  tune the anyon occupation in the vicinity of the charge degenerate lines on which phase slips occur[11].

The vertical nature of the phase slip lines is a consequence of the instantaneous and irreversible nature of the quasipar-

ticle addition events. Indeed, repeated measurement of the interference in the regime of Fig 1d shows that the location of the phase slips changes between measurements (see supplement). An illustration of this is offered by Fig. 2a, which shows an interference plot in a similar regime to Fig. 1d. In these plots, the  $V_P$  is fixed while  $V_C$  is swept rapidly to vary the interferometer area and produce an interference pattern, while the magnetic field is ramped from minimum to maximum over 33 minutes. As in Fig. 1d, a series of discrete slips are observed. However, in this comparatively rapid measurement, phase slips do not occur until the magnetic field has already been increased by 70 mT, nearly 20 minutes after the beginning of the measurement. This is evidenced by the continuous Aharonov-Bohm phase evolution at low  $B$ , which reflects the changing flux through a loop of fixed anyon charge and approximately fixed size. Reversing the direction of the  $B$  sweep (Fig. 2b) reveals a symmetric, and thus hysteretic, behavior where phase slips start only after the field is *lowered* sufficiently. Evidently, the location of a given phase slip in our experiment is not an equilibrium property, but depends on the history of the system. This suggests that the anyon occupation  $N_{qp}$  is out of equilibrium with the sample edge.

Hysteretic behavior of this type can be understood as a consequence of slow charge dynamics. As illustrated in Fig. 2c, slow charging leads to a discrepancy between the equilibrium value of the chemical potential,  $\mu_{eq}$ , which is set by the gate voltages and magnetic field, and the actual chemical potential of the graphene layer  $\mu(t)$ . This effect is not completely unexpected, as long charging times are a characteristic of quantum Hall systems[49, 50], including within quantum Hall gaps in similarly fabricated graphene devices[51]. In the supplement, we use integer quantum Hall interference at  $\nu = -1$  at  $B \approx 4$  T to measure the bulk quasiparticle charging time,  $\tau$ , directly. We find that the charging time grows rapidly as the chemical potential moves deeper into the transport plateau, with phase slips (in the integer regime, arising completely from bulk-edge coupling) transitioning from reversible to hysteretic as  $\tau$  becomes longer than the measurement time.

### QUASIPARTICLE DYNAMICS IN $\nu = 1/3$

The slow charging allows quasiparticle dynamics to be studied at *fixed* magnetic field, using only a single gate voltage to measure both the interference phase and quasiparticle dynamics. Fig. 3a shows data taken at  $B = 9$  T as a function of  $V_C$ . In this measurement,  $V_C$  is swept over a range spanning  $\sim 10$  oscillations in  $\approx 30$  seconds. The range of this raster is adjusted from trace to trace, so that the average value of  $V_C$  increments slowly over  $\sim 30$  minutes. Most successive traces show identical oscillatory patterns, but a pattern of abrupt phase slips is again evident. Fig. 3b shows the phase  $\theta$  of each trace extracted from the discrete Fourier transform. Notably, no background subtraction is necessary at constant  $B$ . We observe 18 phase slips over this range with a mean

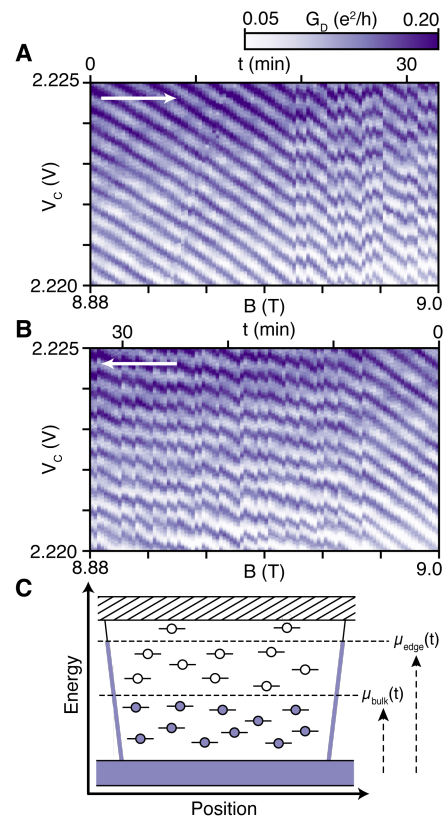
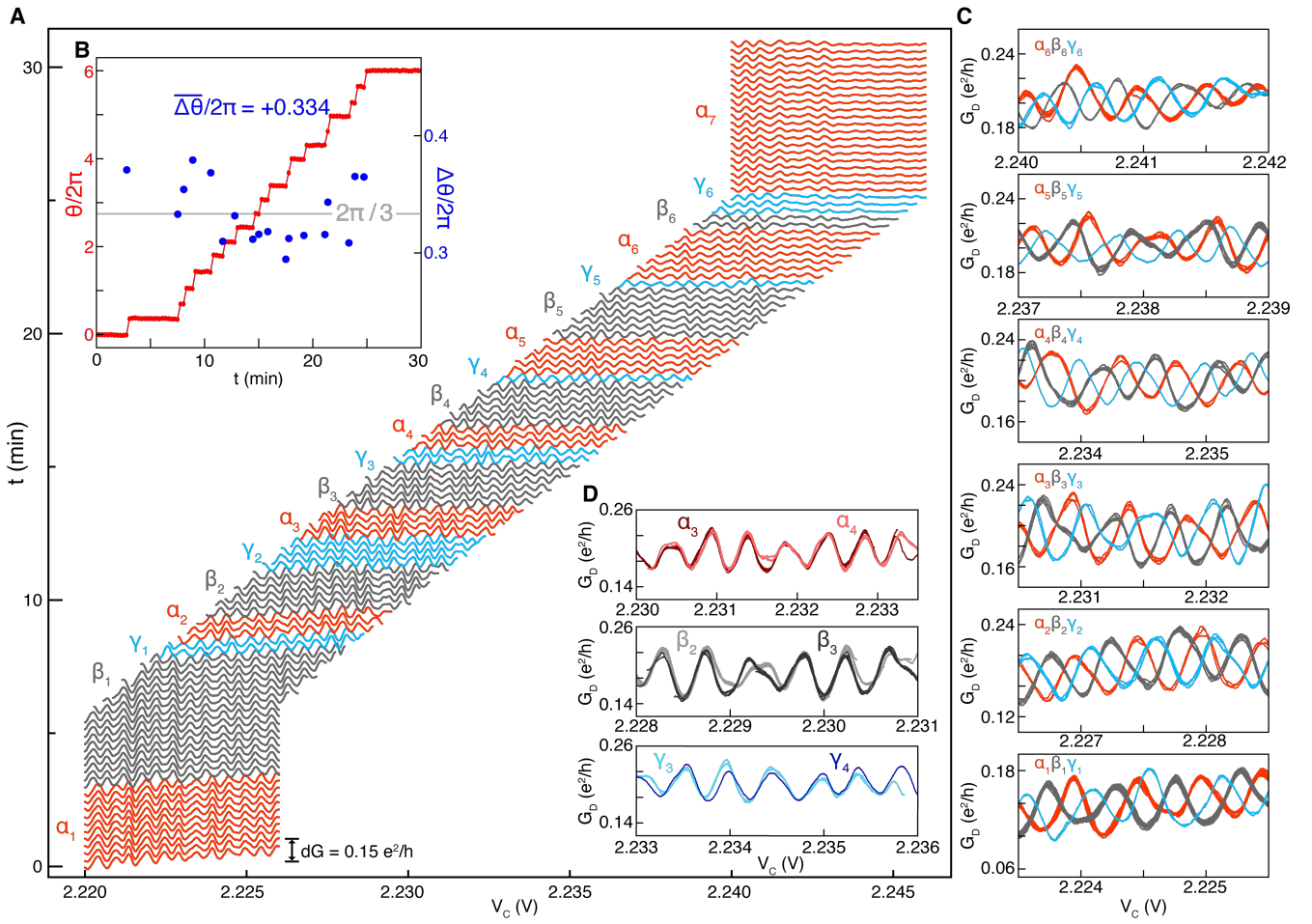


FIG. 2. **Irreversible charging dynamics.** (A)  $G_D$  vs.  $V_C$  as the magnetic field is swept from 8.88T to 9T. The latter half of the measurement shows many sudden phase jumps, beginning at  $B = 8.95$  T and continuing until the end of the sweep. (B)  $G_D$  vs.  $V_C$  as the magnetic field is swept from 9T to 8.88T. Now, the sudden phase jumps differ in exact location, number, and magnitude, not beginning until  $B < 8.97$  T and again continuing until the end of the sweep. (C) Localized states within the fractional quantum Hall energy gap have slow tunneling rates to the gapless edge; as a result, the chemical potential of the electrically isolated bulk ( $\mu_{bulk}$ ) lags the chemical potential of the edge ( $\mu_{edge}$ ) during a ramp of the magnetic field or gate voltage. In this schematic, purple indicates filled states.

value of  $2\pi \times 0.334$  and a standard deviation of  $2\pi \times 0.038$ .

We interpret each of these slips as the entry of a single anyon into the interferometer. We correspondingly collect traces into groups where the phase is the same, and label these by a Greek letter  $\{\alpha, \beta, \gamma\}$  corresponding to  $N_{qp} \bmod 3$ . A numerical subscript distinguishes traces with the same  $N_{qp} \bmod 3$  that are separated by 3 phase slips; assuming each phase slip corresponds to entry of a single fractionally-charged quasiparticle, these traces correspond to charge configurations differing by an integer number of whole electron charges in the interferometer. Fig. 3c compares traces  $\{\alpha_i, \beta_i, \gamma_i\}$  for  $i = \{1, \dots, 6\}$ . Each comparison shows a clear ‘triple-helix’ pattern arising from the  $2\pi/3$  relative phase shift between each set of curves.

Within an individual panel of Fig. 3c, all curves are measured under identical conditions of magnetic field and applied



**FIG. 3. Addition of individual  $e/3$  quasiparticles at constant field (A)** Repeated line traces of the conductance  $G_D$  plotted as a function of  $V_C$ . Traces are vertically offset by an amount proportional to the time between the start of each trace. The window over which  $V_C$  is swept gradually increases over time, favoring an increase in the number of quasiparticles. Interpreting each phase slip as the addition of a single anyon, the traces are grouped into distinct classes  $\alpha$ ,  $\beta$ , and  $\gamma$  corresponding to the respective values of  $N_{qp} \bmod 3$ . **(B)** The phases extracted from the Fourier transform of each trace in panel A are plotted in red. Each phase jump is assumed to lie in the interval  $(-\pi, \pi)$ . Blue points correspond to the magnitude of each sudden jump in  $\theta$ . **(C)** Collections of line traces from each set of three adjacent classes  $\alpha_i, \beta_i, \gamma_i$  plotted over the region where the data overlap in  $V_C$ . The stability of the phase is apparent given the overlap between traces within a given class, while the classes are offset from each other by a  $\sim 2\pi/3$  phase shift. **(D)** Collections of line traces from classes which are separated by three phase slips. These pairs of classes have an indistinguishable phase, but small differences in the exact shape of the curves are apparent.

gate voltages. As might be expected, traces taken at different times but for the same total charge show excellent reproducibility. A less obvious question is whether addition of a whole electron modifies the  $G_D - V_C$  relation; in particular, if that electron is added deep in the bulk, it is not expected to detectably affect the interferometer phase. Indeed, comparison of data separated by three quantized phase slips show no discernible change in the oscillation *phase*, as illustrated in Fig. 3d. Notably, however, traces differing by a whole electron—e.g.,  $\alpha_3$  and  $\alpha_4$ —are distinguishable through deviations in the precise *amplitude* of individual interference fringes. This effect is robust across nearly all groups of traces separated by a  $2\pi$  phase shift in Fig. 3 (see supplement). We speculate that this ‘charge fingerprint’ encoded in the fringe intensities arises from the exponential sensitivity of transmission through our

quantum point contacts to their electrostatic environment—including the electrical potential generated by the addition of even a gate-screened electrical charge in the bulk.

Because the pattern of oscillation amplitudes provides information about the charge configuration not contained in the oscillation phase alone, it allows us, under certain conditions, to determine the absolute phase (interpreted as the total electron charge in the interferometer [52]) rather than just the phase modulo  $2\pi$ . This allows us to distinguish quasiparticle entry and exit under static experimental conditions in the time domain. Fig. 4a shows the result of ramping the magnetic field to a set point and then, starting from  $t = 0$ , leaving it constant for 35 minutes while continuing to repeatedly ramp  $V_C$  over a small ( $\sim 1.5$  mV) range. Several phase slips are visible over the course of the experiment, separating regions of stable

phase which we label I-VII in Fig. 4b. Were the phase jumps assumed to fall into the interval  $(-\pi, \pi)$ , their nearly consistent magnitudes could lead to the assumption that every jump corresponds to the addition of one quasiparticle, as is energetically favored by the reduction in total flux at the beginning of the measurement.

However, a close examination of the measured conductance (Fig. 4c) shows the fringe intensity patterns in regions II and V to be indistinguishable; regions I and IV are also identical after noting that the phase slip occurs midway through the single trace that comprises region IV. This leads us to identify these regions with a return to the same charge configuration as well as the same absolute phase. In fact, equating the regions which have an indistinguishable ‘charge fingerprint’ necessitates that at least one of the first 3 phase slips must correspond to a *removal* of two quasiparticles, rather than the naïve interpretation of every slip as the addition of a single quasiparticle. Fig. 4C shows two possible corrected traces of  $\theta(t)$ , with the light and dark blue traces differing from the uncorrected  $\theta$  by a shift of  $-2\pi$  at the second or third phase slip, respectively.

The time dependence of the quasiparticle number implied by either of these possibilities reconciles our earlier observation of the identical ‘charge fingerprints’ in *both* regions I and IV, and regions II and V. The information required to discriminate between the two possibilities is provided by the magnitude of the phase slip from region II to region III: here,  $\Delta\theta$  is significantly *larger* than  $\theta_a$ , whereas a finite amount of bulk-edge coupling should only serve to decrease the magnitude of the phase jump. (All of the other phase slips show a value slightly less than  $\theta_a$ ). This suggests that the slip separating regions II and III should be associated with a decrease in the number of quasiparticles by two, as the change in phase is then  $\Delta\theta = -4\pi/3 + \delta\theta_{BE}$ .

The observed relaxation dynamics depend strongly on the preparation and operating regimes of the system. As shown in the supplementary material, measurements in similar ranges to those shown in Figs. 3a and 4a can be made to show zero phase slips over several hours for suitable choice of state preparation, despite the flux in the interferometer loop being modulated by several flux quanta. These results imply that for certain impurities, at least, equilibration times are considerably in excess of twenty minutes. As described in the supplementary material, other preparation-dependent anomalies may arise: running the measurement sequence of Fig. 3a in reverse immediately following that measurement reveals no phase slips as  $V_C$  is decreased across the same range, but for a different preparation history, a sequence of phase slips is observed as a function of *decreasing*  $V_C$  with magnitude most easily attributed to the correlated entry of two quasiholes near the sample edge per phase slip.

## DISCUSSION

The exceptionally slow quasiparticle dynamics of our interferometer open new routes to quantitatively probe the physics

of fractionalized phases at the single anyon level. Measuring few-anyon dynamical processes via the response of the interferometric phase to both  $\theta_a$  and Coulomb effects may give new insight into states where inter-quasiparticle correlations are important, such as in the formation dynamics of anyonic Wigner crystal states, as well as the hierarchical fractional quantum Hall states.

The observed time-dependence of  $N_{qp}$  also raises questions about the dynamics in the  $1/3$  state that we have not addressed here. One question concerns the mechanism of the time-dependent fluctuations in  $N_{qp}$ , as observed in Fig. 4C. For instance, these events may be driven by some internal mechanism, such as random quantum tunneling of quasiparticles between sharply-confined disorder sites, or an external effect such as the random absorption of high-energy photons.

Recent advances in spatial imaging techniques, allowing high resolution charge sensing in dual-gated devices[53], may be used to help resolve these questions. Applied to interferometer devices of a similar construction to ours, this may allow direct correlation between the real-space distribution of localized anyons and the interferometric phase. Such experiments could also provide information on the consequences of the real-space disorder present in van der Waals devices on both equilibrium and non-equilibrium models of bulk-edge coupling.

Graphene heterostructures also exhibit even denominator fractional quantum Hall states expected to host non-Abelian anyons[27, 28, 54], raising the question of whether interferometry experiments of this type will be similarly enlightening in such states. In bilayer graphene, energy gaps for the even denominator states have been found to be comparable in size to those of the  $1/3$  state studied in the present work[30, 31], likely leading to similarly slow dynamics for the charged  $e/4$  quasiparticles in those states. A key outstanding question concerns the timescale for motion of the charge-*neutral* excitations that encode the fermion parity. While this timescale must ultimately be determined by experiment, the exceptionally long timescales for charge motion reported here lend hope that unambiguous detection of non-Abelian statistics may be within reach.

*Note Added:* During the preparation of this manuscript, we became aware of a concurrent work using a similar graphene device [55].

## DATA AVAILABILITY

The data that support the findings of this study are available from the corresponding author upon reasonable request.

## ACKNOWLEDGEMENTS

The authors acknowledge helpful discussions with T. Wang, S. Kivelson and S. Das Sarma. Work at UCSB was primarily supported by the Office of Naval Research under

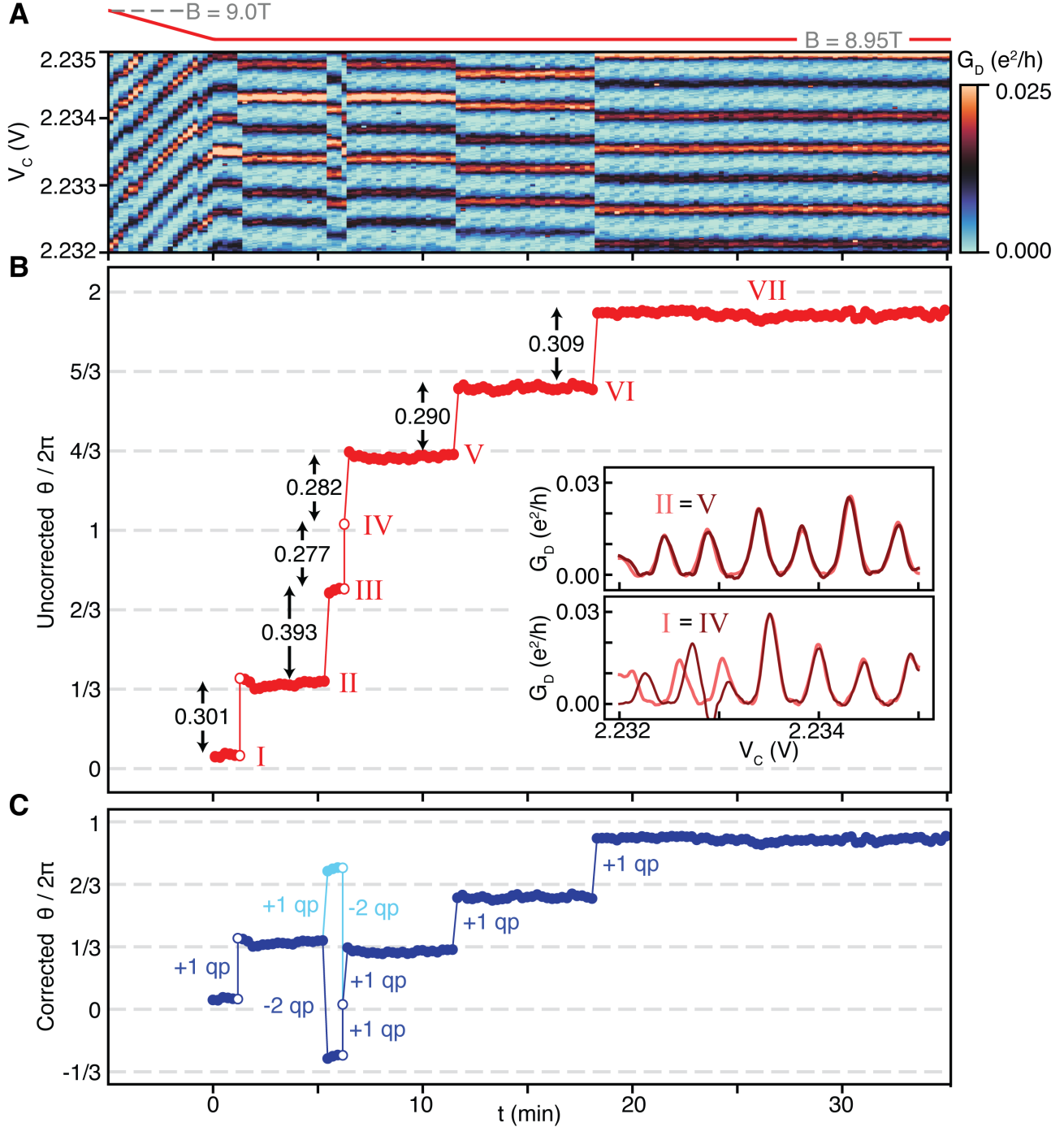


**FIG. 4. Time domain reconstruction of the quasiparticle occupation** (A) Repeated measurement of  $G_D$  over a fixed window of  $V_C$ . At the beginning of the measurement, the magnetic field is swept from 9.0T to 8.95T, where it is subsequently held constant for 35 min. (B) The phase,  $\theta$ , extracted from the Fourier transform of the data in panel A. Each jump is assumed to be in the interval  $\Delta\theta \in (-\pi, \pi)$ . For traces in which a phase jump is observed in the middle of the line trace, two points are plotted as open circles, corresponding to the two values of phase extracted before and after the jump. Inset: Line traces of  $G_D$  taken from regions II and V, showing the indistinguishability not only in phase but also in amplitude. Line traces taken from regions I and IV show a similar overlap, after the phase jump occurs mid-line in trace IV. (C) Two versions of the corrected phase,  $\theta$ , identical to the data from panel B except with a shift of  $-2\pi$  applied to either the jump from II to III (dark blue), or the jump from III to IV (light blue). Either modification brings the time dependence of  $\theta$  into accordance with the interpreted changes in  $N_{qp}$  (marked for each curve) by matching the 'charge fingerprints' of regions I and IV, and regions II and V.

award N00014-23-1-2066. Development of fabrication based on anodic oxidation lithography were supported by the Air Force Office of Scientific Research under award FA9560-20-1-0208. AFY acknowledges additional support by the Gordon and Betty Moore Foundation EPIQS program under award GBMF9471. LC and NS received additional support from the Army Research Office under award W911NF20-1-0082. MZ was supported by the U.S. Department of Energy, Office of Science, Office of Basic Energy Sciences, Materials Sciences and Engineering Division under Contract No. DE-AC02-05-CH11231 (Theory of Materials program KC2301). K.W. and T.T. acknowledge support from JSPS KAKENHI (Grant Numbers 19H05790, 20H00354 and 21H05233).

\* These authors contributed equally to this work

† andrea@physics.ucsb.edu

- [1] J. M. Leinaas and J. Myrheim, *Il Nuovo Cimento B* **37**, 1 (1977).
- [2] F. Wilczek, *Physical Review Letters* **49**, 957 (1982).
- [3] D. Arovas, J. R. Schrieffer, and F. Wilczek, *Physical Review Letters* **53**, 722 (1984).
- [4] B. I. Halperin, *Physical Review Letters* **52**, 1583 (1984), publisher: American Physical Society.
- [5] G. A. Goldin, R. Menikoff, and D. H. Sharp, *Journal of Mathematical Physics* **21**, 650 (1980), publisher: American Institute of Physics.
- [6] S. Kivelson, *Physical Review Letters* **65**, 3369 (1990).
- [7] C. d. C. Chamon, D. E. Freed, S. A. Kivelson, S. L. Sondhi, and X. G. Wen, *Physical Review B* **55**, 2331 (1997).
- [8] E.-A. Kim, *Physical Review Letters* **97**, 216404 (2006), publisher: American Physical Society.
- [9] B. I. Halperin, A. Stern, I. Neder, and B. Rosenow, *Physical Review B* **83**, 155440 (2011).
- [10] N. Read and S. Das Sarma, *Nature Physics* **20**, 381 (2024).
- [11] J. Nakamura, S. Liang, G. C. Gardner, and M. J. Manfra, *Nature Physics* **16**, 931 (2020).
- [12] J. Nakamura, S. Liang, G. Gardner, and M. Manfra, *Physical Review X* **13**, 041012 (2023).
- [13] F. E. Camino, W. Zhou, and V. J. Goldman, *Phys. Rev. B* **72** (2005).
- [14] F. E. Camino, W. Zhou, and V. J. Goldman, *Physical Review Letters* **98**, 076805 (2007).
- [15] Y. Zhang, D. T. McClure, E. M. Levenson-Falk, C. M. Marcus, L. N. Pfeiffer, and K. W. West, *Physical Review B* **79**, 241304 (2009).
- [16] D. T. McClure, Y. Zhang, B. Rosenow, E. M. Levenson-Falk, C. M. Marcus, L. N. Pfeiffer, and K. W. West, *Physical Review Letters* **103**, 206806 (2009).
- [17] N. Ofek, A. Bid, M. Heiblum, A. Stern, V. Umansky, and D. Mahalu, *Proceedings of the National Academy of Sciences* **107**, 5276 (2010).
- [18] H. K. Choi, I. Sivan, A. Rosenblatt, M. Heiblum, V. Umansky, and D. Mahalu, *Nature Communications* **6** (2015), 10.1038/ncomms8435.
- [19] I. Sivan, H. K. Choi, J. Park, A. Rosenblatt, Y. Gefen, D. Mahalu, and V. Umansky, *Nature Communications* **7**, 12184 (2016).
- [20] J. Nakamura, S. Fallahi, H. Sahasrabudhe, R. Rahman, S. Liang, G. C. Gardner, and M. J. Manfra, *Nature Physics* **15**, 563 (2019).
- [21] R. Willett, K. Shtengel, C. Nayak, L. Pfeiffer, Y. Chung, M. Peabody, K. Baldwin, and K. West, *Physical Review X* **13**, 011028 (2023).
- [22] J. Nakamura, S. Liang, G. C. Gardner, and M. J. Manfra, *Nature Communications* **13**, 344 (2022).
- [23] C. R. Dean, A. F. Young, P. Cadden-Zimansky, L. Wang, H. Ren, K. Watanabe, T. Taniguchi, P. Kim, J. Hone, and K. L. Shepard, *Nature Physics* **7**, 693 (2011).
- [24] H. Polshyn, H. Zhou, E. M. Spanton, T. Taniguchi, K. Watanabe, and A. F. Young, *Physical Review Letters* **121**, 226801 (2018).
- [25] Y. Zeng, J. I. A. Li, S. A. Dietrich, O. M. Ghosh, K. Watanabe, T. Taniguchi, J. Hone, and C. R. Dean, *Physical Review Letters* **122**, 137701 (2019).
- [26] C. Dean, P. Kim, J. I. A. Li, and A. Young, in *Fractional Quantum Hall Effects: New Developments* (World Scientific, Singapore, 2020) pp. 317–375.
- [27] A. A. Zibrov, C. Kometter, H. Zhou, E. M. Spanton, T. Taniguchi, K. Watanabe, M. P. Zaletel, and A. F. Young, *Nature* **549**, 360 (2017).
- [28] J. I. A. Li, C. Tan, S. Chen, Y. Zeng, T. Taniguchi, K. Watanabe, J. Hone, and C. R. Dean, *Science*, eaa02521 (2017).
- [29] A. A. Zibrov, E. M. Spanton, H. Zhou, C. Kometter, T. Taniguchi, K. Watanabe, and A. F. Young, *Nature Physics* **14**, 930 (2018).
- [30] Y. Hu, Y.-C. Tsui, M. He, U. Kamber, T. Wang, A. S. Mohammadi, K. Watanabe, T. Taniguchi, Z. Papic, M. P. Zaletel, and A. Yazdani, “High-Resolution Tunneling Spectroscopy of Fractional Quantum Hall States,” (2023), arXiv:2308.05789 [cond-mat].
- [31] A. Assouline, T. Wang, H. Zhou, L. A. Cohen, F. Yang, R. Zhang, T. Taniguchi, K. Watanabe, R. S. Mong, M. P. Zaletel, and A. F. Young, *Physical Review Letters* **132**, 046603 (2024).
- [32] C. Déprez, L. Veyrat, H. Vignaud, G. Nayak, K. Watanabe, T. Taniguchi, F. Gay, H. Sellier, and B. Sacépé, *Nature Nanotechnology* **16**, 555 (2021).
- [33] Y. Ronen, T. Werkmeister, D. Haie Najafabadi, A. T. Pierce, L. E. Anderson, Y. J. Shin, S. Y. Lee, Y. H. Lee, B. Johnson, K. Watanabe, T. Taniguchi, A. Yacoby, and P. Kim, *Nature Nanotechnology* **16**, 563 (2021).
- [34] L. Zhao, E. G. Arnault, T. F. Q. Larson, Z. Iftikhar, A. Seredinski, T. Fleming, K. Watanabe, T. Taniguchi, F. Amet, and G. Finkelstein, *Nano Letters* **22**, 9645 (2022).
- [35] H. Fu, K. Huang, K. Watanabe, T. Taniguchi, M. Kayyalha, and J. Zhu, *Nano Letters* **23**, 718 (2023).
- [36] J. Kim, H. Dev, R. Kumar, A. Ilin, A. Haug, V. Bhardwaj, C. Hong, K. Watanabe, T. Taniguchi, A. Stern, and Y. Ronen, “Aharonov-Bohm interference and the evolution of phase jumps in fractional quantum Hall Fabry-Perot interferometers based on bi-layer graphene,” (2024), arXiv:2402.12432 [cond-mat].
- [37] L. A. Cohen, N. L. Samuelson, T. Wang, K. Klocke, C. C. Reeves, T. Taniguchi, K. Watanabe, S. Vijay, M. P. Zaletel, and A. F. Young, *Nature Physics* **19**, 1502 (2023).
- [38] X.-G. Wen, *Physical Review B* **44**, 5708 (1991).
- [39] C. L. Kane and M. P. A. Fisher, *Physical Review Letters* **68**, 1220 (1992).
- [40] P. Fendley, H. Saleur, and N. P. Warner, *Nuclear Physics B* **430**, 577 (1994).
- [41] C. L. Kane and M. P. A. Fisher, *Physical Review B* **51**, 13449 (1995).



- [42] P. Fendley, A. W. W. Ludwig, and H. Saleur, *Physical Review Letters* **74**, 3005 (1995).
- [43] F. P. Milliken, C. P. Umbach, and R. A. Webb, *Solid State Communications* **97**, 309 (1996).
- [44] I. P. Radu, J. B. Miller, C. M. Marcus, M. A. Kastner, L. N. Pfeiffer, and K. W. West, *Science* **320**, 899 (2008).
- [45] L. A. Cohen, N. L. Samuelson, T. Wang, T. Taniguchi, K. Watanabe, M. P. Zaletel, and A. F. Young, *Science* **382**, 542 (2023).
- [46] Y. Yamauchi, M. Hashisaka, S. Nakamura, K. Chida, S. Kasai, T. Ono, R. Leturcq, K. Ensslin, D. C. Driscoll, A. C. Gossard, and K. Kobayashi, *Physical Review B* **79**, 161306 (2009).
- [47] T. Werkmeister, J. R. Ehrets, Y. Ronen, M. E. Wesson, D. Najafabadi, Z. Wei, K. Watanabe, T. Taniguchi, D. E. Feldman, B. I. Halperin, A. Yacoby, and P. Kim, “Strongly coupled edge states in a graphene quantum Hall interferometer,” (2023), arXiv:2312.03150 [cond-mat].
- [48] B. Rosenow and B. I. Halperin, *Physical Review Letters* **98**, 106801 (2007).
- [49] R. K. Goodall, R. J. Higgins, and J. P. Harrang, *Phys. Rev. B* **31**, 6597 (1985).
- [50] J. P. Eisenstein, L. N. Pfeiffer, and K. W. West, *Phys. Rev. Lett.* **68**, 674 (1992).
- [51] F. Yang, A. A. Zibrov, R. Bai, T. Taniguchi, K. Watanabe, M. P. Zaletel, and A. F. Young, *Physical Review Letters* **126**, 156802 (2021).
- [52] D. E. Feldman and B. I. Halperin, *Physical Review B* **105**, 165310 (2022), publisher: American Physical Society.
- [53] H. Li, S. Li, E. C. Regan, D. Wang, W. Zhao, S. Kahn, K. Yumigeta, M. Blei, T. Taniguchi, K. Watanabe, S. Tongay, A. Zettl, M. F. Crommie, and F. Wang, *Nature* **597**, 650 (2021).
- [54] D.-K. Ki, V. I. Fal’ko, D. A. Abanin, and A. F. Morpurgo, *Nano Letters* **14**, 2135 (2014).
- [55] T. Werkmeister, J. R. Ehrets, M. E. Wesson, D. H. Najafabadi, K. Watanabe, T. Taniguchi, B. I. Halperin, A. Yacoby, and P. Kim, *ArXiv* (2024).
- [56] C. von Keyserlingk, S. Simon, and B. Rosenow, *Physical Review Letters* **115**, 126807 (2015).

## MATERIALS AND METHODS

### S1. Sample Fabrication

Samples 1 and 2 (optical images shown in Fig. S1A,C) were both fabricated using the standard van der Waals dry-transfer process combined with electrode-free AFM anodic oxidation lithography of the graphite top gates before stacking, as described in reference [37]. The structures patterned into each top graphite gate are shown in the AFM topographs of Fig. S1B,D. These scans were acquired in the middle of the stacking process, imaging the exposed graphite top gate after picking it up. After stacking, the device is transferred onto a conductively-doped Si substrate with 285 nm of thermally-grown SiO<sub>2</sub> on the surface.

A mask is defined via E-Beam Lithography (EBL) of a polymethyl methacrylate A4 495K/A2 950K bilayer resist, and 40 nm of aluminum is deposited onto the device to be used as a hard etch mask. The whole stack is then etched through using a CHF<sub>3</sub>/O<sub>2</sub> plasma reactive ion etch for several minutes. The aluminum mask is removed by submersion in a <3% TMAH solution (AZ300MIF) for 20 minutes. Then, a contact electrode pattern is defined using a PMMA 950K A8 mask and another EBL exposure, a 30 second CHF<sub>3</sub>/O<sub>2</sub> RIE etch is performed to clean the expose device edges, and edge contacts are deposited by E-Beam evaporation of 5/15/150nm Cr/Pd/Au layers.

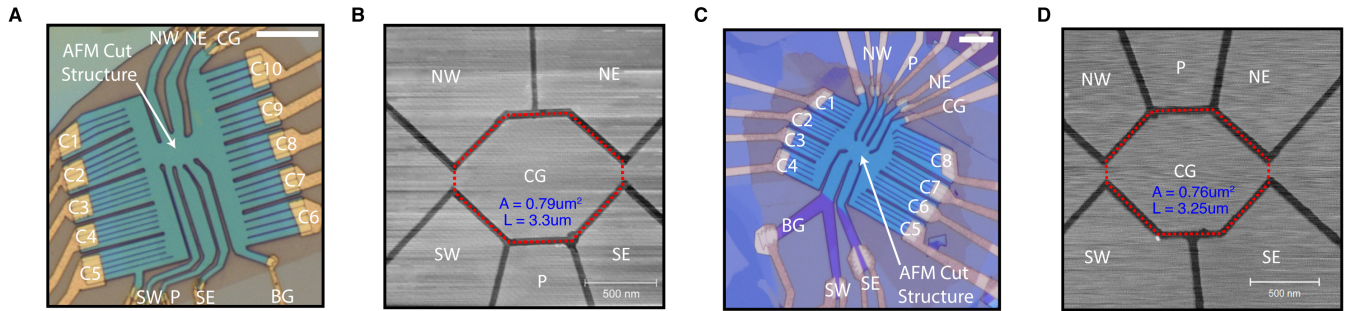


**FIG. S1. Device Images and AFM Cut Gates** (a) Optical micrograph of device 1, the device studied in the main text. Electrical edge contacts to the monolayer are labeled as C1-10. Electrical edge contacts to the gate layers, NW, SW, NE, SE, P, CG, and BG are marked respectively. Scale bar inset is 10  $\mu\text{m}$ . (b) AFM topograph on a transfer slide of the top gate layer after pick-up with an hBN flake. The gate regions shown in panel a, as well as in Fig. 1a, are marked. The measured lithographic area, defined by the perimeter drawn in the red dashed line, is measured to be  $0.79(5) \mu\text{m}^2$ , and the perimeter is measured to be  $3.3(1) \mu\text{m}$ . The uncertainty comes from the width of the etched region in the graphite top gate (it is unknown as to where exactly the edge state is located). (c) Optical micrograph of device 2, a nearly identical device as studied in the main text which we used to perform experiments in the integer quantum Hall regime. Electrical edge contacts to the monolayer are labeled as C1-8. Electrical edge contacts to the gate layers, NW, SW, NE, SE, P, CG, and BG are marked respectively. Scale bar inset is 10  $\mu\text{m}$ . (d) AFM topograph on a transfer slide of the top gate layer after pick-up with an hBN flake for the device in panel c. The gate regions shown in panel c are marked. The measured lithographic area, defined by the perimeter drawn in the red dashed line, is measured to be  $0.76(5) \mu\text{m}^2$ , and the perimeter is measured to be  $3.25(10) \mu\text{m}$ . The uncertainty comes the same source as in panel b.

### Voltages for Main Text Figures

Main Text Figure	$V_{CG}$	$V_{BG}$	$V_{NW/SW}$	$V_{NE/SE}$	$V_P$
Fig. 1c (blue trace)	2.23V	-2V	2.23V	-4.1V	2.23V
Fig. 1c (red trace)	2.23V	-2V	0.5V	2.23V	2.23V
Fig. 1d	2.23V	-2V	0.5V	-4.1V	N/A
Fig. 2a	N/A	-2V	1.0V	-3.2V	2V
Fig. 3	N/A	-2V	1.0V	-3.2V	2V
Fig. 4	N/A	-2V	0.3V	-3.94V	2V

FIG. S2. Fixed voltage set points for main text figures

### S2. Measurement parameters and interferometer characterization

Experiments were performed in a dry dilution refrigerator at a base temperature of 18 mK (on device 1) and 55 mK (on device 2). Electronic filters are installed on all transport lines to lower the electron temperature. Transport was measured at 10.3875 Hz (device 1) / 17.7777 Hz (device 2) using SR860 lock-in amplifiers. A Basel Precision Instruments SP983c high stability I to V converter (IF3602) is used to measure the current signals, while the voltages are measured directly with the SR860 using no additional pre-amplification.

For the diagonal conductance measurements performed on device 1, in the fractional quantum Hall regime, an ac excitation is applied to contacts C6, C7, C8, and C9 and the resulting current  $I_{out}$  is measured on contact C1. The diagonal voltage drop  $V_+ - V_-$  is measured between contacts C10 and C2. A constant 10 V is applied to the conductively-doped Si substrate throughout all measurements to maintain electron-doping in the single- and un-gated regions of each contact. The excitation voltage is  $10 \mu\text{V}$  for the data in Fig. 1D and Fig. 4, and  $20 \mu\text{V}$  for Fig. 2A-B, and Fig. 3.

For the measurements of device 2 in the integer quantum Hall regime, a two-ground configuration is employed. A  $0.9 \text{ nA}$  ac current bias is applied at contact C6, and the contact C8 is grounded to sink the current reflected by the interferometer. The transmitted current is measured on the opposite side of the device, on contact C4. A constant  $-12 \text{ V}$  is applied to the Si substrate throughout these measurements to maintain hole-doping of the contact regions.

As described in the main text, we perform several standard characterizations of our Fabry-Perot interferometer to confirm normal operation, shown in the figures that follow.

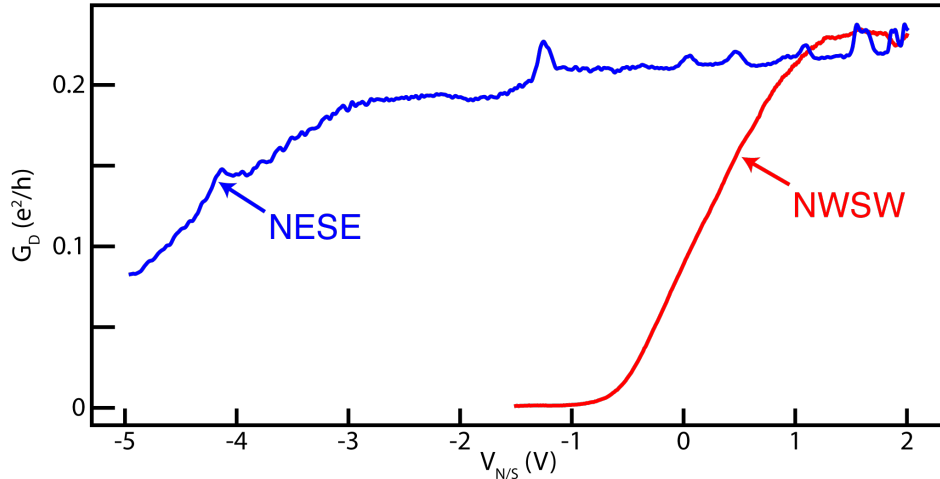


FIG. S3. Individual QPC pinch-off curves in  $\nu = 1/3$ . Blue curve is  $G_D$  vs.  $V_{NE/SE}$  while  $V_{NW/SW}$  is set such that  $\nu_{NW/SW} = 1/3$ . Red curve is  $G_D$  vs.  $V_{NW/SW}$  with  $V_{NE/SE}$  set such that  $\nu_{NE/SE} = 1/3$ . Operating points for both QPCs relevant to the interference data shown in Fig. 1d are identified by the inset arrows.

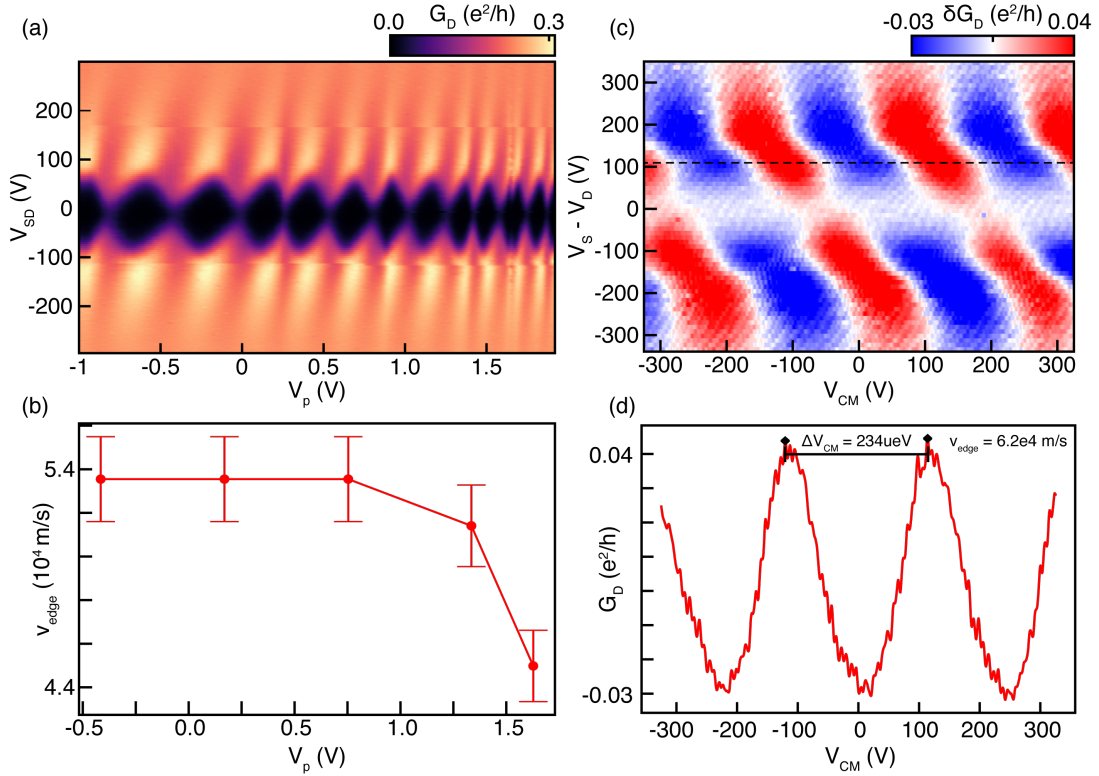


FIG. S4. **Bias and Common Mode Dependence of Interference in  $\nu = 1/3$**  (a)  $G_D$  versus  $V_P$  and  $V_{SD}$  near  $\nu = 1/3$ ,  $B = 9\text{T}$ ,  $V_{CG} = 2.27\text{V}$ ,  $V_{NW/SW} = -0.23\text{V}$ ,  $V_{NESE} = -4.25\text{V}$ . The interference shows a strong suppression of  $G_D$  near zero DC bias, characteristic of chiral Luttinger liquid behavior near the QPCs. Additionally, the interference exhibits a phase-shift resulting from an applied  $V_{SD}$ . Notably, the periodicity in  $V_{SD}$  is reduced for values of  $V_P < 0.5\text{V}$ . (b) Extracted Edge velocity from the periodicity in  $V_{SD}$  in panel a versus  $V_P$ , here we use the formula  $h v_{edge}/\nu L = e\Delta V_{SD}$ . As  $V_P$  becomes enhanced the edge velocity exhibits a 19% reduction coming from the decreasing sharpness of the confinement potential near the plunger gate. (c)  $\delta G_D$  as a function of both the common mode voltage on the monolayer,  $V_{CM}$ , and the difference between the voltages on the source and drain terminals relative to fridge ground,  $V_S - V_D$ ; this difference is taken by varying the voltage on  $V_S$  while keeping  $V_D$  fixed. This data is taken in the same operating regime as Fig. 1d. The periodicity in  $V_{CM}$  directly tells us  $e/C_I$ , and consequently the edge velocity as quoted in the main text. (d) Line cut along the dashed black line in panel c. We can extract the peak-to-peak distance between fringes versus  $V_{CM}$ , which yields a periodicity  $\Delta V_{CM} = 234 \mu\text{V}$ . Using the relation  $h v_{edge}/\nu L = e\Delta V_{CM} = e^2/C_I$ , we find that  $v_{edge} = 6.2 \times 10^4$  m/s. Despite the fact the panels a-b and panels c-d are taken at slightly different gate voltages we observe good agreement with the predicted edge velocity for the  $\nu = 1/3$  edge mode using two different methods.

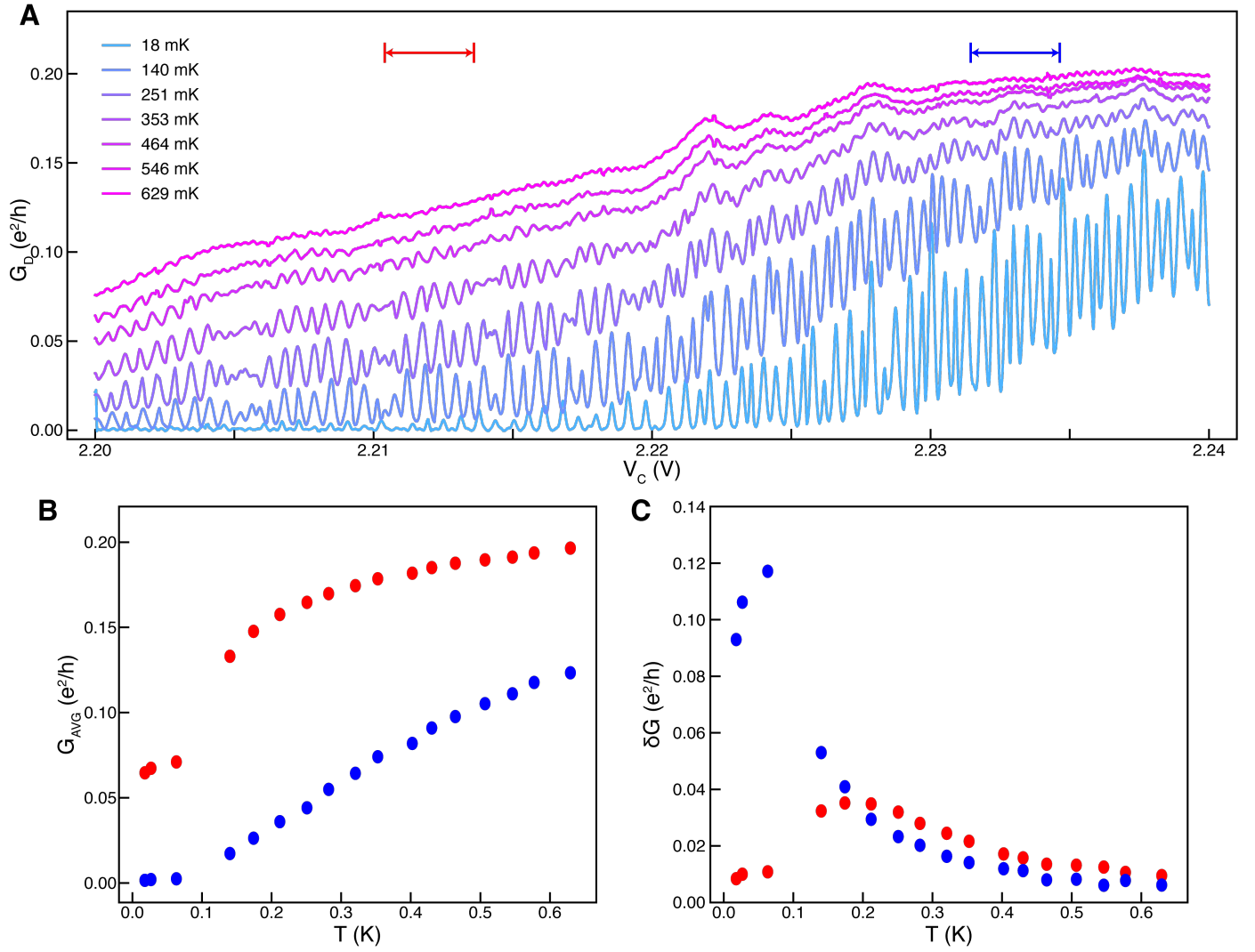
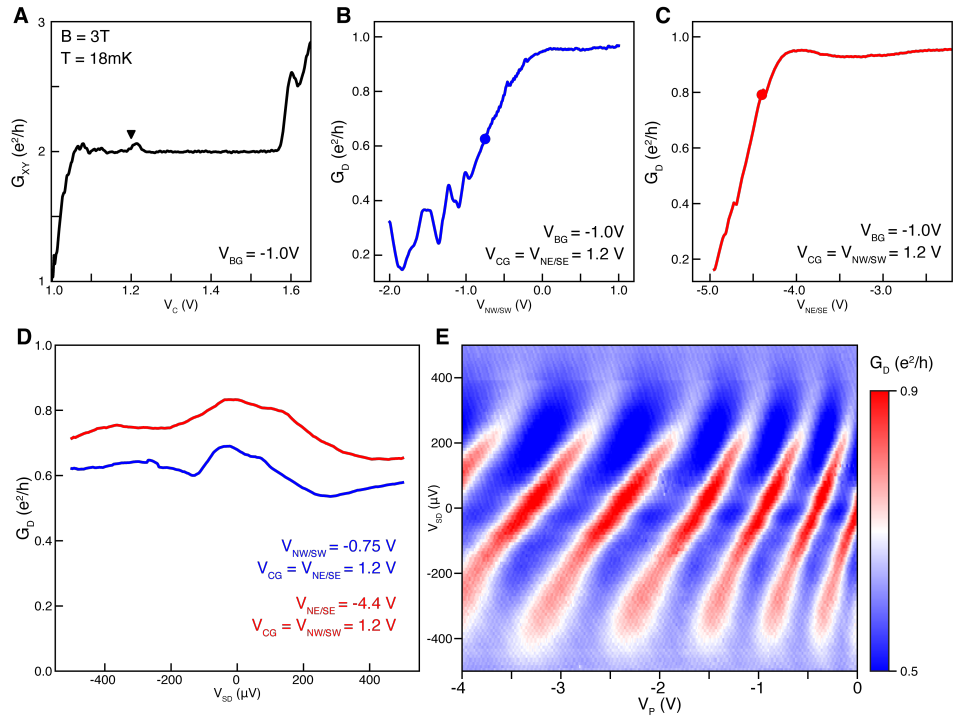


FIG. S5. **Temperature dependence in FQH (device 1)** (a)  $G_D$  versus  $V_C$  in  $\nu = 1/3$ , with both QPCs at partial pinch off, showing clear oscillations for a range of temperatures measured on our sample probe between  $T = 18$  mK and  $T = 639$  mK. (b) The average value of the diagonal conductance,  $G_{AVG}$ , plotted versus the temperature on the probe  $T$  for two ranges in  $V_C$  marked by the red and blue arrows respectively in panel a. The average value reflects the tunneling rate of the two QPCs, which for a chiral Luttinger liquid is expected to change significantly with increasing temperature. (c) Visibility, denoted as  $\delta G$  and defined as the average difference between successive maxima and minima in the interference is plotted versus the temperature on the probe,  $T$ . Interestingly, the interplay between the chiral Luttinger liquid renormalization of the QPC transmission and the temperature induced decoherence of the interference leads to a maximum in the visibility that depends on the initial set point of  $V_C$ .



**FIG. S6. Bias Dependence of the QPC transmission in the outer edge of the  $\nu = 2$  state (device 1).** (A) Hall conductance as a function of  $V_C$  at 3T. The interferometer is characterized in the  $\nu = 2$  state with the center gate fixed at the marked point. (B, C) Diagonal conductance across the device with each QPC pinched off individually. (D) Dependence of the transmission through each QPC at the marked points in B,C on the applied source-drain DC bias  $V_{SD}$ . No zero-bias suppression in the conductance is observed, in stark contrast to the phenomenology observed in the FQH regime. (E) Dependence of the interference on the source drain bias and plunger gate, with both QPCs set to the marked points in B,C simultaneously.

### S3. Phase Slip Magnitude Analysis

To extract the magnitudes of the phase slips reported in Fig. 1e we start by subtracting off the mean value of  $G_D$  for each line-trace versus  $V_P$  at a fixed value of  $B$ . We then take the 1D discrete Fourier transform (DFT) along the  $V_P$  axis of the data in Fig. S7a (the mean subtracted data from main text Fig. 1d). The absolute value of the resulting DFT is shown in Fig. S7b. We then extract the phase from the component of the DFT which has the largest absolute magnitude, here around 3 cycles per volt of  $V_P$ . The point-to-point difference in the phase, extracted in this way, as a function of  $B$  contains a nearly constant background, as expected for a linear phase accumulation from the Aharonov-Bohm effect. However, this constant background is interrupted by sharp spikes at the location of each sudden phase slip.

To remove the Aharonov-Bohm effect and purely extract the value of the sudden phase slips, we take a moving trimmed mean in a 7-point window (ignoring outliers bigger than  $|\Delta\theta| = 0.4$ ) of the point-to-point difference of the phase versus  $B$ . This enables us to extract a rough estimate of the background. This rough background is fit to a line, and then further refined with a new trimmed mean of the original point-to-point difference (with the same window size). The refined trimmed mean excludes outliers greater than the fit value at fixed  $B$  plus  $\Delta\theta = 0.14$  or less than the fit value minus  $\Delta\theta = 0.17$ . The integrated phase (plotted in red) including the sudden slips, along with the integrated background (plotted in black), is shown in Fig. S7c. Subtracting the integrated phase from the integrated background produces the dataset shown in Fig. S7d where the phase jumps are isolated. The outlier exclusion range at the refinement step is set to guarantee the Fourier analysis reproduces the number of observed phase slips in Fig. S7a.

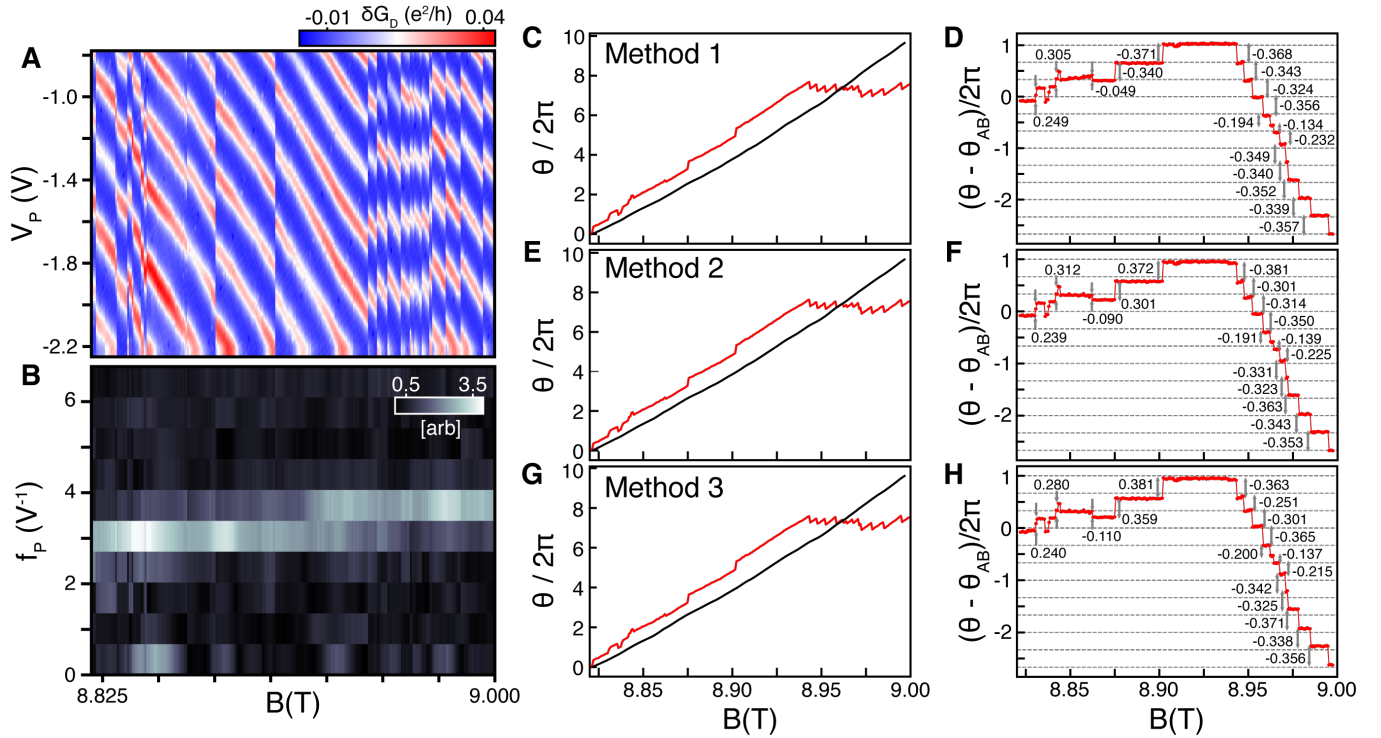


FIG. S7. **Extracting Phase Slip Magnitudes** (a) Same data as in main text Fig. 1d, but with the mean value of  $G_D$  for each value of magnetic field subtracted from the corresponding trace versus  $V_P$ . (b) Absolute magnitude of the discrete 1D Fourier transform (along  $V_P$ ) of the data in panel a plotted versus magnetic field and inverse  $V_P$ . (c, e, g) The integrated  $\theta$  vs.  $B$  extracted from the DFT is plotted in red. The integrated background, which we subtract off from the accumulated phase to calculate the magnitude of the phase slips, is plotted in black. Panel c shows the integrated phase and the integrated background extracted from the DFT by taking the phase of the largest magnitude component; this is the analysis method we use for all phase slip extractions in the main text. Panel e shows the same data as panel c, but the phase is extracted by taking a weighted average over the peak in the DFT amplitude. Panel g shows the same data as panels c and e, but the phase is extracted by taking an unweighted average over the peak in the DFT amplitude. (d)  $\theta - \theta_{AB}$  versus magnetic field extracted by subtracting the integrated background from the integrated phase calculated via the method in panel c. This data is identical to the main text Fig. 1e. (f) Same as panel d, but the phase slip magnitudes are calculated from the data in panel e. (h) Same as panels f and d, but the phase slip magnitudes are calculated from the data in panel g.

While it is true that the calculated phase slip magnitudes weakly depend on the choice of the trimmed mean exclusion range, the variation is limited to the standard deviation in the point-to-point phase difference after coarsely removing the phase slips

using the same criterion as the initial trimmed mean (outliers with  $|\Delta\theta| > 0.4$  are removed). We find that  $\sigma_{\Delta\theta} = 2\pi \cdot 0.012$ ; leading to an uncertainty of  $2\pi \cdot 0.012 \cdot \sqrt{2} = 2\pi \cdot 0.017$  for the magnitude of a sudden phase slip. While this is small compared to the magnitude of the observed jumps, it is not the dominant source of error in our measurement. As can be seen by the resulting DFT in Fig. S7b, the peak in the DFT amplitude spectrum has some finite width; this is ultimately the result of the interference signal not being perfectly periodic in  $V_P$ . Consequently, there is some freedom in the analysis method used to determine the phase of the primary DFT component which introduces some systematic error beyond the statistical contribution.

To roughly quantify the size of this systematic uncertainty, we chose two additional analysis methods and checked the processed phase slip magnitudes against the method used in the main text. The second method we used was to take a weighted average of the phase, weighted by the normalized absolute magnitude of the DFT signal, around the peak in the DFT between  $f_P = 2 V^{-1}$  and  $f_P = 5 V^{-1}$ . An identical set of panels to Fig. S7c-d where the phase jumps are extracted using the weighted average (method 2), are shown in Fig. S7e-f. The third method we used (method 3) was to take an unweighted average of the DFT phase across the same range in method 2. Similarly to Fig. S7c-f, the integrated phase and background, as well as the extracted phase slips, are plotted in Fig. S7g-h. We find that for each phase slip, the typical deviation between the three methods is  $|\delta(\Delta\theta)| < 2\pi \cdot 0.01$ . However, for some phase slips the deviation can be as large as  $\pm 2\pi \cdot 0.037$  between methods. Since we cannot check every possible analysis method, we will take our global systematic uncertainty to be the largest observed deviation (across all phase slips in Fig. S7a) from the average across the three methods; we find this to be  $\pm 2\pi \cdot 0.04$ .

We use the same method outlined in the beginning of this section (method 1) to extract the sudden phase slip magnitudes for all other relevant datasets. It's important to note that while the statistical uncertainty from the background subtraction is not relevant to other datasets, such as Fig. 3 and Fig. 4, where no Aharonov-Bohm component needs to be subtracted off, we expect the systematic uncertainty from the Fourier analysis persists. Consequently, for datasets where we analyze phase shifts with no background component, we still assume our uncertainty is  $\sigma_{\Delta\theta} \approx \pm 2\pi \cdot 0.04$ .



#### S4. Bulk-edge and exterior-edge coupling at $\nu = \frac{1}{3}$

The edge ‘‘capacitance.’’ In the main text we reported the common-mode periodicity  $\Delta V_{CM} = 234 \mu\text{V}$ , which we relate to the capacitance of the edge as  $e = \Delta V_{CM} C_I$ . This measurement is taken in the regime where the bulk is completely incompressible (no phase slips). But we should note that in the notation of Halperin et al. [9], this measurement is more properly understood as a characterization of  $K_I = 234 \mu\text{eV}$ . When the bulk is entirely incompressible, the relation between the two is trivial:  $K_I = e^2/C_I$ . However, if extended to the regime when the bulk is compressible (for example at a phase slip), and with finite-bulk edge coupling  $K_{IL}$ , the parameters are related as a matrix inverse  $K = e^2 C^{-1}$ , so that  $C_I = \frac{e^2}{K_I - K_{IL}^2/K_L}$ . We do not expect  $K_I$  to depend too much on the bulk filling, while  $C_I$  will depend on the filling via quantum capacitance effects in  $K_L$ . Thus when we refer to  $C_I$  as ‘‘the capacitance of the edge,’’ strictly speaking this should be understood as  $e^2/K_I$ . In any case the capacitance matrix is not so relevant to our experiments because the bulk and edge are out of equilibrium.

Bulk-edge coupling of the anyonic phase. We elaborate on the derivation of Eq.(2) of the main text, which gives the Coulomb coupling between an anyonic impurity and the edge. Assuming the radius of curvature of the edge is large compared with the impurity distance, we can treat the edge as a line with capacitance per unit length  $C_I/L$ . The induced charge is then  $\delta Q_I = \frac{C_I}{L} \frac{e}{3} \int G(x, R) dx$  where  $G$  is the double-gated Green’s function with a charge  $e/3$  at  $(x, y) = (0, R)$ . Making use of the effective translation variance along  $x$ , we can then use a conformal transformation to find that a 1D line charge  $\rho$  produces a potential  $\phi(y) = \frac{\rho}{2\pi\sqrt{\epsilon_{xy}\epsilon_z}} \log(\tanh(\pi y \sqrt{\epsilon_z/\epsilon_{xy}}/4d)) \approx \frac{1}{\pi\sqrt{\epsilon_{xy}\epsilon_z}} e^{-\pi y \sqrt{\epsilon_z/\epsilon_{xy}}/2d}$ . This gives the estimate  $\delta Q_I = \frac{e}{3} \frac{C_I}{\pi\sqrt{\epsilon_{xy}\epsilon_z} L} e^{-\pi y \sqrt{\epsilon_z/\epsilon_{xy}}/2d}$ . This also provides an estimate of the average bulk-edge coupling,  $K_{IL} = \frac{e^2}{A} \int_{y>0} \int dx G(x, y) dx dy = \frac{e^2}{2A} \frac{d}{2\epsilon_z} = \frac{e^2}{2Ac_g}$ , where  $c_g$  is the geometric bulk capacitance per unit area.

This discussion also points out the need to generalize the analysis of Ref.[9] in order to describe bulk-edge coupling in our experiments. In that work, the bulk was assumed to be in electro-chemical equilibrium and that it could be treated as a single lumped element with charging energy  $K_L$ . In our experiment, however, we are able to resolve charging of single impurities. To explain bulk-edge coupling in this regime requires a more fine-grained model keeping the charge state of each impurity  $a$  and an impurity-edge coupling  $K_{L,a}$ , which is precisely the quantity analyzed above.

Bulk-edge coupling of the AB phase. In Fig. 1 of the main text we found that in the regime of Aharonov-Bohm oscillations in which  $N_{qp}$  is kept fixed, the field period  $\Delta B$  varies from 15 mT to 18 mT as the plunger gate voltage  $V_P$  is varied from  $-0.75 \text{ V}$  to  $-2.25 \text{ V}$ . Assuming pure Aharonov-Bohm evolution,  $\frac{e}{3} A \Delta B = h$ , this gives a range of areas  $A \sim 0.69 - 0.83 \mu\text{m}^2$  in good agreement with the nominal geometric area of the device. Here we discuss two qualifications to this analysis, and their possible resolution:

- The measured *variation* in  $\Delta B$  is larger than can be explained by the  $V_P$ -dependence of  $A$ .
- In the standard theory of bulk-edge coupling,[9] the field period should receive a correction  $\frac{e}{3} \bar{A} (1 - K_{IL}/K_I) \Delta B = h$ , and from theoretical estimates of the  $K_{IL}$  it is surprising the field period is in such good agreement with the nominal area.

We propose that the resolution to both arises from a novel feature of our graphene Fabry-Perot interferometer geometry, which has not been considered in the literature focused on GaAs devices. Specifically, the filling outside the interferometer is of opposite sign to the interior ( $\nu_{\text{ext}} \ll 0$  for positive filling of the interferometer), giving rise to coupling between the edge state and this exterior region we term ‘‘exterior-edge’’ coupling. Exterior-edge coupling counteracts the effect of the typical bulk-edge coupling between the edge state and the interior of the interferometer.

The variation in  $\Delta B$  would at first seem to be intuitive, as  $\theta = \frac{e}{3} A_I(V_P, B) B/\hbar$  and  $V_P$  increases the area  $A_I$ . However, the observation of only 4 interference periods over this range of  $V_P$  implies  $A_I$  has changed by an area of  $4 \cdot 2\pi \ell_B^2/\nu \sim 10^{-3} \mu\text{m}^2$ , which is negligible compared to the observed 20% variation in  $\Delta B$ . We conjecture the  $V_P$  dependence instead occurs through the  $B$ -dependence of  $A_I$ ,  $\partial_B \theta = \frac{e}{3} A_I (1 + B A_I^{-1} \partial_B A_I)/\hbar$ . This dependence is one manifestation of bulk-edge Coulomb coupling: as  $B$  is increased at fixed  $N_{qp}$  (and hence  $\nu$ ), the electron density  $n = \nu e B/\hbar$  in the bulk increases, which in turn tends to shrink the edge due to Coulomb coupling, reducing  $A_I$ . The standard theory [9, 56] of bulk-edge coupling predicts

$$\theta = (1 - \frac{K_{IL}}{K_I} \frac{\nu_{\text{in}}}{\Delta\nu}) e^* \bar{A} B/\hbar \quad (1)$$

where in the present case  $\nu_{\text{in}} = \Delta\nu = 1/3$ ,  $e^* = e/3$ . Here  $K_I \sim e^2/C_I \approx 234 \mu\text{eV}$  describes the compressibility of the edge and  $K_{IL}$  is a phenomenological bulk-edge Coulomb coupling. The change in  $\Delta B$  could then arise from a  $V_P$  dependence of  $K_I$  or  $K_{IL}$ . Based on the electrostatics of a double-gated device, we expect bulk edge coupling of  $K_{IL} = e^2/2c_g A \approx 86 \mu\text{eV}$ , where  $c_g = 2\epsilon_z/d$  is the capacitance to the gates. Furthermore, we have measured  $K_I \sim 234 \mu\text{eV}$  and find it changes by only about 15% as  $V_P$  is varied over an even larger range of  $V_P$  than displayed in Fig 1. The prediction of the standard theory then

raises a puzzle, as the resulting correction by  $(1 - 86/234) \approx 0.63$  would imply that the actual area is in fact  $\sim 60\%$  larger than previously inferred,  $\bar{A} \sim 1.1 - 1.3 \mu\text{m}^2$ . This is at odds with the nominal size of the interferometer  $0.74 - 0.83 \mu\text{m}^2$ .

We conjecture this discrepancy arises from an effect not previously considered in the context of GaAs FPI. In the standard theory of bulk-edge coupling, it is implicitly assumed that  $\nu \rightarrow 0$  within a short distance of the edge. In our graphene FPI, however,  $\nu \sim -5$  in the exterior of the interferometer. As a result we expect additional Coulomb coupling between the charge in the *exterior* of the FPI and the edge. When the exterior is operated in a gap, the exterior charge density will introduce a new term to the Coulomb correction:  $(1 - \frac{K_{IL}}{K_I} \frac{\nu_{\text{in}}}{\Delta\nu} - \frac{K_{I,\text{ext}}}{K_I} \frac{\nu_{\text{ext}}}{\Delta\nu})$ . In double-gated devices, we again estimate  $K_{I,\text{ext}} \sim K_{IL} \sim e^2/2c_g A$  (while it may seem strange for  $K_{I,\text{ext}}$  to depend on  $A$ , this is an artifact of the factor of  $A$  which has been factored out in Eq.(1): for both the bulk and exterior coupling, the important scale is the gate distance relative to the perimeter,  $d/L$ ). For  $\nu_{\text{ext}} < 0$  the exterior charge will thus counteract the bulk-edge coupling. In double-gated devices, fields are screened over a scale  $d$ , so the relevant  $\nu_{\text{ext}}$  is one averaged over a distance of  $\sim d$  from the interfering edge. Over this range we expect the density to fall from  $\nu = \frac{1}{3} \rightarrow -5$  through a series of steps whose spatial structure depends on the details of the electrostatics and interaction energies. It is thus difficult to quantitatively predict  $\nu_{\text{ext}}$ . Nevertheless, this hypothesis can be tested through a future study of the interferometer field period as a function of  $\nu_{\text{ext}}$ , though this requires a modified device design.

### S5. Thermal dephasing of the interference phase in in the FQH regime

As the temperature increases, the amplitude  $\delta G$  of the conductance oscillations is observed to decrease; this is theoretically expected due to dephasing processes. In the FQH case, quantitative analysis of this dependence is complicated by the non-linear  $T, V$  characteristic of the current: the effective back-scattering amplitude of a single quantum-point contact scales as a power-law in  $T$ . [7, 38, 39] At least in the limit of perturbative backscattering, this RG flow can be cancelled by considering the ratio of the oscillation amplitude and the mean current,  $\delta I_B / \bar{I}_B = \delta G_D / (e^2/3h - \bar{G}_D)$  [9]. The result is shown in Fig. S8A, and over a range of  $T$  shows exponential dependence  $e^{-T/T_0}$  with  $T_0 = 87$  mK.

When accounting for thermal fluctuations of the conformal field theory on the edge alone, Ref.[7] predict  $kT_0 = \frac{\hbar v}{\pi \nu L}$  (note their notation for the edge geometry is related to ours by  $a = L/2$ ). Relating this to the measured edge capacitance  $\frac{\hbar v}{\nu L} = \frac{e^2}{C_I} \approx 234 \mu\text{eV}$ , we would then predict  $kT_0 = \frac{e^2}{2\pi^2 C_I} = 137$  mK, in rather poor agreement with our experiment. Here we show the discrepancy with the CFT prediction can be accounted for by including fluctuations in the bulk quasiparticle number, [9] an effect also observed in Ref.[11].

Noting that the interference phase is proportional to the total electron charge  $\theta = 2\pi N$ , the thermal dephasing of  $\langle e^{i\theta} \rangle_T$  arises from fluctuations in  $N$ . The result can then be estimated given the capacitance of the edge  $C_I$  and bulk  $C_L$ . [9] Focusing on an operating point where  $\langle N_{qp} \rangle_T = 0$ , and, for simplicity, ignoring bulk-edge coupling, we obtain

$$\frac{\langle e^{i\theta} \rangle_T}{\langle e^{i\theta} \rangle_0} = \left( \frac{1}{Z_I} \int e^{2\pi i N - \frac{e^2 N^2}{2C_I kT}} dN \right) \left( \frac{1}{Z_B} \sum_{N_{qp}} e^{i2\pi i(N_{qp}/3) - \frac{(e/3)^2 N_{qp}^2}{2C_L kT}} \right) \quad (2)$$

$$\approx e^{-2\pi^2 kT(C_I + C_L)/e^2} = e^{-T/T_0} \quad (3)$$

To obtain the exponential approximation we have taken the high- $T$  limit where fluctuations in  $N_{qp}$  are large; for  $kT < \frac{(e/3)^2}{C_L}$ ,  $N_{qp}$  fluctuations will be frozen out (or un-observable when the equilibration time becomes long). Below we obtain the estimate

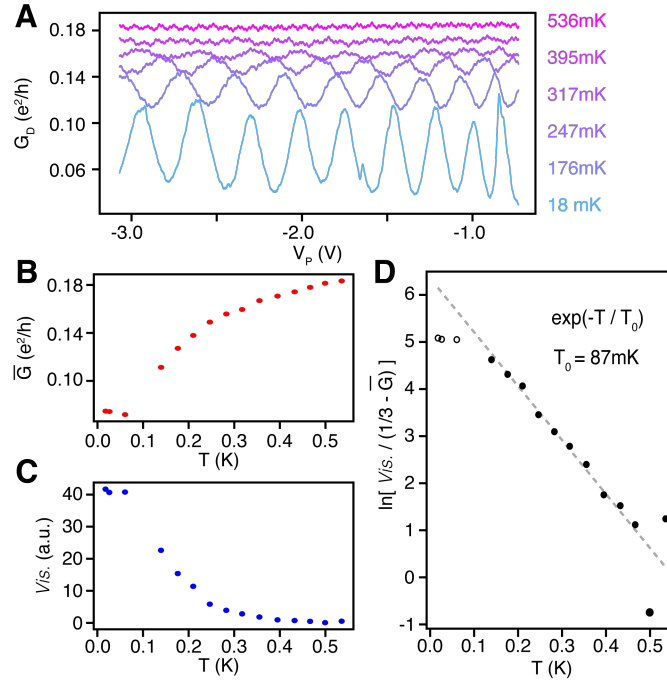


FIG. S8. **Scaling of the interference visibility with temperature, suggesting a finite amount of thermal dephasing from  $N_{qp}$  fluctuations (device 1)** (A)  $G_D$  vs.  $V_P$  oscillations in the  $\nu = 1/3$  state, measured as a function of temperature at fixed  $V_C = 2.230$  V. (B) The average value of the conductance  $\bar{G}$  as a function of temperature shows strong temperature dependence, characteristic of a chiral Luttinger liquid edge. (C) Interference visibility, defined by taking the absolute value of the largest Fourier component of the oscillations at base temperature, and tracking the amplitude of that component as a function of temperature. (D) To cancel the power-law dependence of the backscattering, here we normalize the visibility by the average backscattering across the interferometer,  $(e^2/3h - \bar{G})$ . The normalized visibility exhibits exponential suppression  $e^{-T/T_0}$  from which we extract  $T_0 = 87$  mK

$\frac{(e/3)^2}{C_L} \sim 170$  mK, and experimentally we indeed find good exponential behaviour above this scale. As discussed, using the measured value of  $\frac{e^2}{C_I} = 234 \mu\text{eV}$ , we find that the edge alone contributes  $kT_0 = e^2/2\pi^2 C_I \sim 137$  mK.

Additional fluctuations from  $N_{qp}$  are then needed to explain the measured value, which requires knowledge of the bulk capacitance  $C_L$ . The capacitance of the bulk arises from taking the geometric and quantum capacitance in series,  $C_J^{-1} = C_g^{-1} + C_q^{-1}$ . The quantum capacitance can in turn be related to the electronic compressibility of the device,  $A \frac{e^2}{C_q} = \frac{\partial \mu}{\partial n}$ . Fortunately the compressibility of the MLG 1/3-state was measured by our group in Ref.[51], where we obtained  $\frac{\partial \mu}{\partial n} \approx 0.15 \text{ meV} \mu\text{m}^2$  at  $B = 18$  T (this can be obtained from the published data by extracting the in-gap slope of  $\frac{1}{2\pi\ell_B^2} \frac{\partial \mu}{\partial n} = \frac{\partial \mu}{\partial \nu} \sim 646 \text{ meV}$ ). It remains to convert this to an estimate of the compressibility at the  $B = 9$  T used here. Proceeding phenomenologically, it is reasonable to assume the in-gap density of states arises from quasiparticles pinned to impurity sites. Assuming the spatial density of these states is set by the impurity density, and is hence independent of  $B$ , [31] with energies equally distributed over the FQH gap  $\Delta_{1/3} \propto \sqrt{B}$ , we conclude the compressibility will scale as  $1/\sqrt{B}$ . We thus scale the compressibility by  $\sqrt{9/18}$  to obtain  $\frac{\partial \mu}{\partial n} \approx 0.1 \text{ meV} \mu\text{m}^2$ . The estimated quantum capacitance is then  $\frac{e^2}{C_q} \sim 0.13 \text{ meV}$  using the estimated size  $A \sim 0.8 \mu\text{m}^2$  of the interferometer. The quantum capacitance then adds in series with doubly-gated geometric capacitance  $\frac{e^2}{C_g} = \frac{e^2 \epsilon_s d}{2A} \sim 0.17 \text{ meV}$ : all together, we thus estimate  $\frac{e^2}{C_L} = 0.3 \text{ meV}$ .

Taking the bulk and edge capacitances in parallel, we obtain  $e^2/C_t \sim (1/0.3 + 1/0.234)^{-1} \text{ meV} \sim 0.131 \text{ meV}$ , giving a dephasing temperature  $T_0 = 77$  mK, quite close to the measured value of  $T_0 = 87$  mK. This may be partially a matter of good fortune given the estimates involved in  $C_t$ , but the scales are clearly consistent with a dephasing temperature set by a combination of bulk and edge contributions. In the future this analysis could be made quantitative using devices capable of measuring the capacitance of the center gate defining the interferometer.

### S6. Quasiparticle dynamics and bulk-edge coupling at $\nu = -1$

To further explore the evolution of charge dynamics, and to characterize the role of bulk-edge coupling in the absence of contributions from the anyon phase, we study integer filling of  $\nu = -1$  at range magnetic fields near  $B = 4\text{T}$  in a second device, where the single chiral edge mode of  $\nu = -1$  avoids the complexity inherent in compound edges in higher filling factors [47]. Because no anyon phase slips are expected at  $\nu = -1$ , we can attribute the observed phase jumps entirely to changes in interferometer area via the bulk-edge coupling [9].

Figs. S9a-c show interference data taken in three regions of the  $\nu = -1$  transport plateau, approaching the plateau center from the high filling-factor side. Note that for  $\nu = -1$ , depleting the interferometer area requires applying a positive voltage to  $V_P$ ,

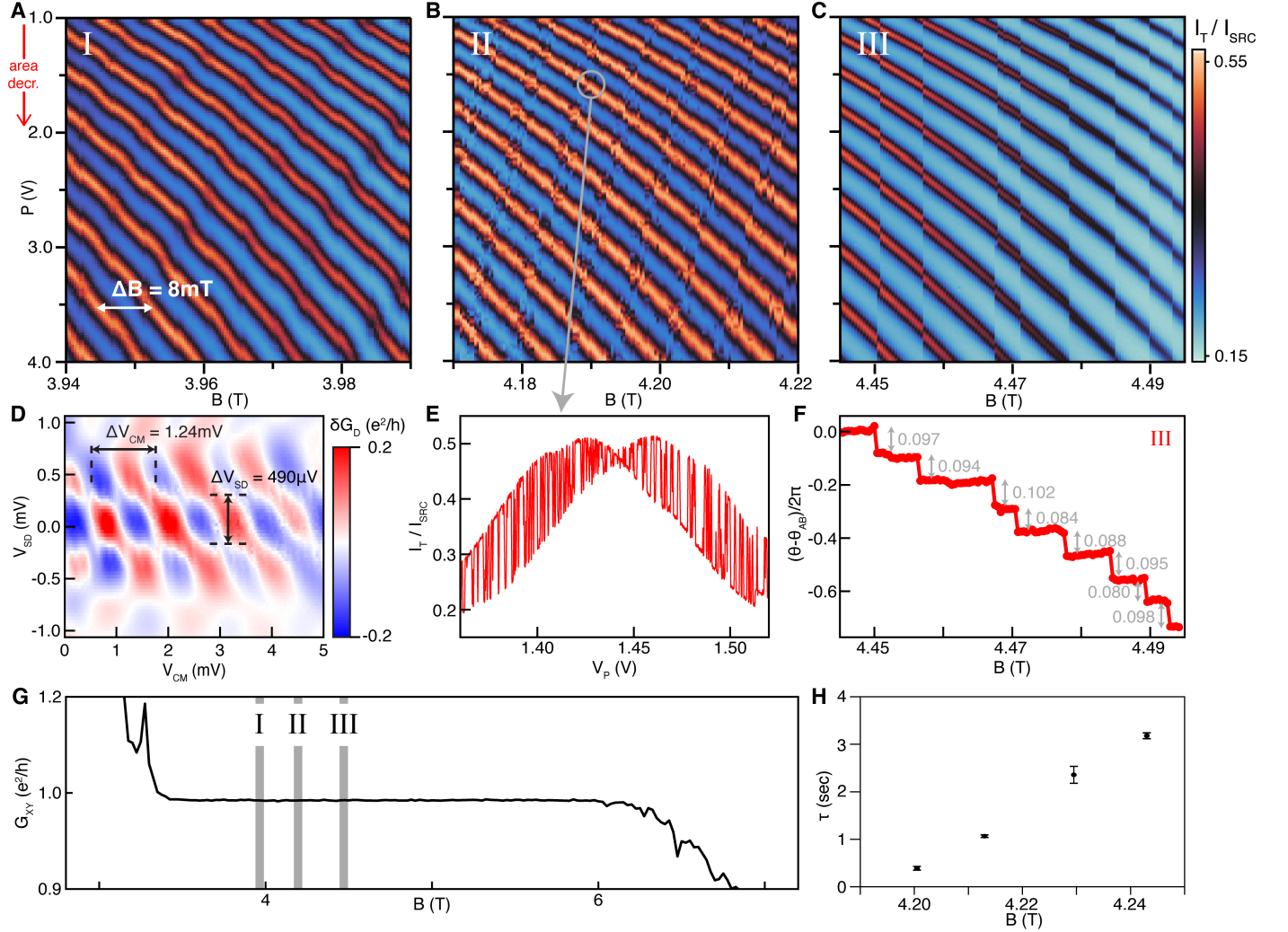


FIG. S9. **Continuous evolution of the quasiparticle charging time at  $\nu = -1$  (device 2).** (A) The transmitted current across the interferometer as a function of the plunger gate voltage,  $V_P$ , and magnetic field  $B$ , measured at a fixed electron density, with  $V_B = 0.3\text{V}$  and  $V_C = -0.580\text{V}$  corresponding to the  $\nu = -1$  plateau near  $B \approx 3.96\text{ T}$ . The interference is Aharonov-Bohm dominated throughout. The phase slip behavior evolves from continuous in this field range to (B) noisy near  $B \approx 4.2\text{ T}$  to (C) discrete near  $B = 4.47\text{ T}$ . (D) Dependence of the differential diagonal conductance on the applied DC source-drain bias,  $V_{SD}$ , applied to the source contact, and a common-mode voltage  $V_{CM}$ , applied to both the source and drain contacts (E) A representative trace of the transmission vs. plunger gate voltage  $V_P$  at the point circled in panel B. Clear switching behavior between two phase-offset curves is observed. (F) The phase  $\theta$  as a function of  $B$ , extracted from the Fourier Transform of panel C. The median phase difference between successive traces is subtracted to remove the smooth evolution of the Aharonov-Bohm phase. The remaining discrete jumps have a characteristic value of  $\Delta\theta/2\pi = -0.092 \pm 0.008$ . (G) Measurement of  $R_{xy}$  on the W side of the device at  $V_C = -0.580\text{V}$  and  $V_B = 0.3\text{V}$ . The grey boxes mark the field ranges I, II, and III in which interference data of panels A, B, and C were taken, respectively. (H) Evolution of the quasiparticle switching rate as a function of magnetic field inside the “noisy” regime. The error bar plotted is the value of the asymmetry of the 1-to-2 and 2-to-1 switching rates,  $\Delta\tau = |\tau_{12} - \tau_{21}|$ .

so the negative slope of the constant-phase lines is consistent with Aharonov-Bohm dominated interference, and the observed field period  $\Delta B = 8 \text{ mT}$  implies an effective area of approximately  $A_I = 0.52 \mu\text{m}^2$  when ignoring bulk-edge coupling, slightly smaller than the lithographic area of  $A = 0.76 \mu\text{m}^2$  (as discussed in a previous section, the quantitative discrepancy may arise from bulk-edge coupling).

In Fig. S9a, we observe regular phase slips that are reversibly tuned by both plunger gate and magnetic field, spaced by approximately one flux quantum. This is consistent with the breathing of the interferometer area due to the repeated entry of single electron quasiparticles each with a small but finite bulk-edge coupling of approximately the same magnitude. As these data are taken near the edge of the transport plateau, we expect the system to have a finite compressibility, and the quasiparticle states to be relatively delocalized.

In addition, the measurement of the interference signal as a function of the dc common mode voltage  $V_{CM}$  allows us to estimate the expected degree of bulk-edge coupling as done in section S4. From the measured common-mode period  $\Delta V_{CM}$  at  $B = 4.0 \text{ T}$ ,  $K_I = e\Delta V_{CM} = 1.24 \text{ meV}$ . The geometric capacitance of the island can be approximated from the thickness of the hBN spacers (45 nm each) and measured lithographic area  $A_I$  of the graphite top gate, leading to an estimated (following section S4) of  $K_{IL} = e^2/2c_g A \approx 89 \mu\text{eV}$ . Thus, the expected phase shift from the bulk edge coupling is  $\delta\theta_{BE}/2\pi = K_{IL}/K_I = 0.072$ . This is in agreement with the size of the observed phase slips within our systematic uncertainty.

As we increase the magnetic field and move closer to the center of the plateau, we observe a striking qualitative change in the interference signal near the phase slip lines. In Fig. S9B, while the pattern of phase slips remains regular, telegraph-noise develops in the transmitted current near the charge degeneracy line associated with each phase slip. This is illustrated in Figs. S9E, which shows a trace of the transmitted current as a function of  $V_P$ , acquired slowly over the course of 36 seconds across the marked charge-degeneracy point. Evidently, the transmission through the interferometer switches between two distinct patterns offset by a small phase shift on a few-100ms timescale. As we increase the magnetic field further towards the center of the  $\nu = -1$  plateau, the switching behavior becomes less apparent, and we recover sudden and irreversible phase slips as described in the fractional quantum Hall regime in the main text: interference data show lines of continuously evolving AB phase interrupted by sharp, irregularly spaced phase slips that are instantaneous and irreversible (Fig. S9C). In contrast to the fractional quantum Hall regime, however, the magnitude of these phase slips is much smaller than  $2\pi/3$ , with  $\Delta\theta/2\pi \approx -0.092 \pm 0.04$  for the slips shown in Fig. S9C - slightly greater than the estimated equilibrium value but consistent within our relatively large systematic uncertainty. However, a larger effect from bulk-edge coupling is not unexpected as some bulk states may be physically closer to the edge than others contributing to a larger observed change in  $A_I$  upon loading.

Evidently, the charge equilibration time  $\tau$  varies strongly over a small magnetic field range, going from faster than 10 ms (the time to acquire a single pixel in Figs. S9A-C) to slower than 7s (the time to acquire a complete line in Fig. S9A-C) over a range of 500 mT. This increase can be quantified precisely in the regime of Fig. S9B, where the switching time  $\tau \approx 1 \text{ s}$ . The plotted values of the characteristic time  $\tau$  are plotted in Fig. S9H, illustrating a sharp and monotonic increase over a very narrow range of 45 mT.

To extract the data-points in Fig. S9H, we analyze the telegraph noise quantitatively using a two-state switching model where our readout is the interference signal at distinct charge-degenerate points for several values of B. Fig. S10a shows a measurement of the transmitted current illustrating roughly the location of one of the measured charge-degenerate lines in the switching-noise regime. Precisely at the charge degeneracy point, we expect the tunneling rate to have some characteristic time  $\tau$ . In general, however, we expect the ratio  $P_{1\rightarrow 2}/P_{2\rightarrow 1} = e^{-\Delta/k_b T}$ , where  $P_{1\rightarrow 2}$  is the probability for an electron to hop from state 1 to state 2,  $P_{2\rightarrow 1}$  is the probability for the electron to hop from state 2 to 1, and  $\Delta$  is the detuning away from the charge degeneracy point. As a result, the location of the charge-degenerate point in  $V_P - B$  plane must be determined systematically by measuring the switching noise as a function of the detuning.

Fig. S10B shows the characteristic values of the transmitted current  $I_T$  between which the signal switches, extracted from 20-minute measurements of the transmitted current while fixed at each point, along the illustrated line from A to B in Fig. S10A. The charge degenerate point is determined by plotting the fraction of time spent in state 1,  $P(1)$ , as function of the plunger gate voltage, plotted in Fig. S10C.

Fig. S10G-L show histograms of the two dwell times,  $\tau_1$  and  $\tau_2$ , for different plunger gate voltages near a phase slip line, showing a strong dependence of the relative rates on detuning. For a given B, we identify the the value of  $V_P$  where  $\tau_{12} \approx \tau_{21}$  as the charge degeneracy point, and plot  $\tau \equiv (\tau_{12} + \tau_{21})/2$  in Fig. 3I, with the difference  $\Delta\tau \equiv |\tau_{12} - \tau_{21}|$  as the error bar. We find that  $\tau$  increases by nearly one order of magnitude over a 45 mT range of magnetic fields.

The dramatic slowing of charge dynamics within the plateau is not unexpected: as the filling factor moves closer to the center of the  $\nu = -1$  plateau, quasiparticle states are increasingly localized around impurity sites. Individual impurity orbitals will, consequently, be increasingly far from the sample edge. The dramatic resulting difference in  $L$ -dependence allows  $\tau$  to change dramatically while the bulk edge coupling remains nearly unchanged. For example, reducing the radius of an impurity state centered 100 nm from the edge will increase  $\tau \sim 1/\Gamma$  by three orders of magnitude, while only changing the bulk edge coupling by 15%.

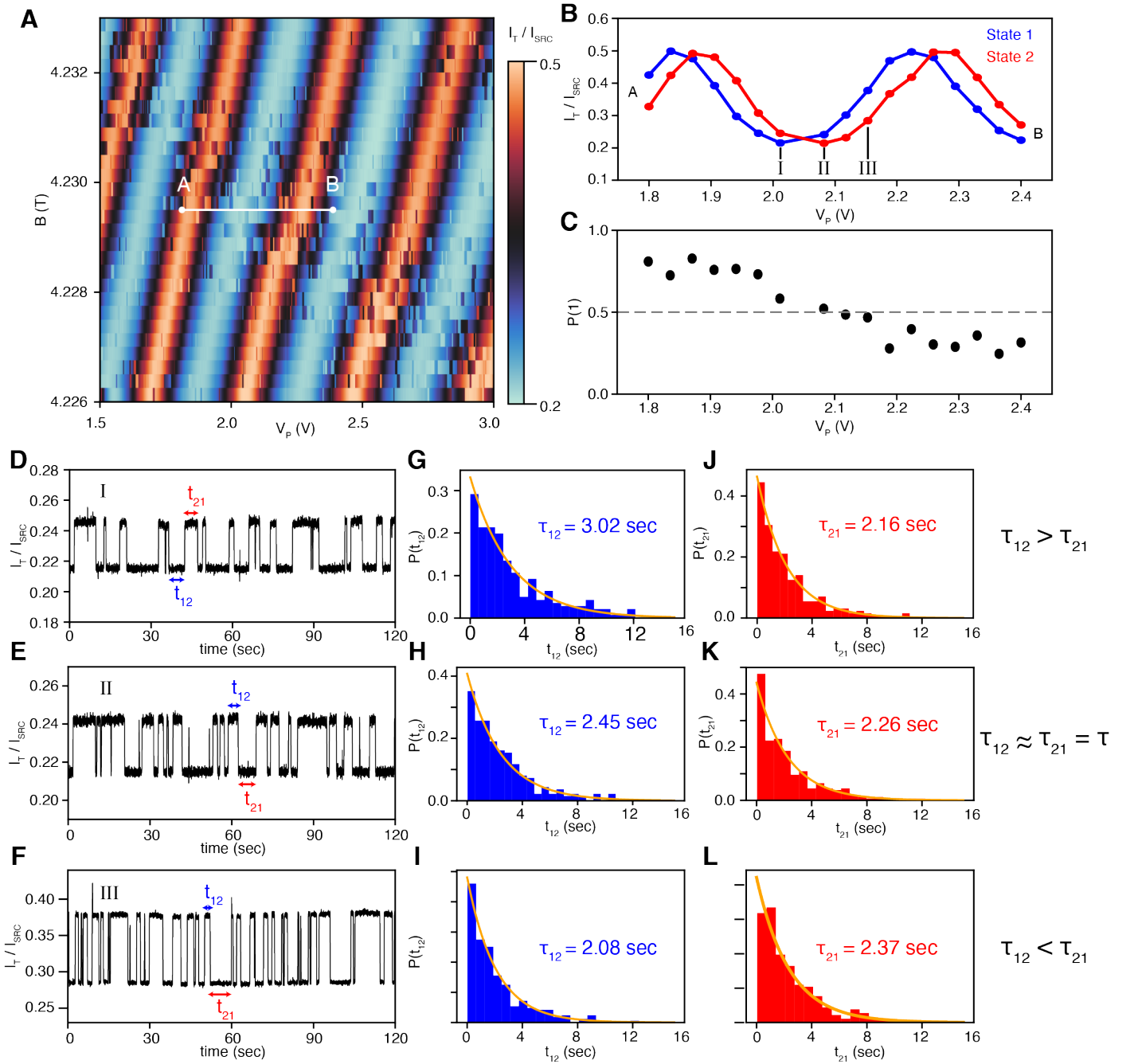


FIG. S10. **Analysis of the quasiparticle switching rate in the switching-noise regime in  $\nu = -1$**  (A) Measurement of the interference pattern in the transmitted current across a single charge degeneracy line in the switching noise regime of  $\nu = -1$ . (B) The median current in each of the two stable configurations in the switching noise regime. The median value of  $I_T$  in each state, plotted in red and blue, are extracted from 20 minute measurements of the current at each fixed  $V_P$ , by splitting the histogram of the acquired data into two halves at the midpoint and taking the median value of current for each half. (C) The fractional probability to occupy state 1 at each plunger gate voltage in B, acquired by simply taking the number of data points lying on either side of the halfway-point threshold between the two stable values of current. The charge degeneracy point is defined as the point at which  $P(1)$  crosses 0.5. (D,E,F) Three examples of the time-dependent current data used to extract the dwell times  $\tau_{12}$  and  $\tau_{21}$ . (G,H,I) Histograms of the dwell times in state 1,  $t_{12}$ , each showing an exponential distribution with a characteristic time  $\tau_{12}$  that decreases as the charge degeneracy line is crossed from left to right. (J,K,L) Histograms of the dwell times in state 2,  $t_{21}$ , showing that the characteristic time  $\tau_{21}$  increases as the charge degeneracy line is crossed from left to right.

### S7. SHARPLY CONFINED CHARGE TRAPS AND FULL RANGE OF DATA IN FIGURE 1

Expanding the range of data presented in the main text Fig. 1d we observe two phase slips which are continuously tuned with both  $B$  and  $V_P$ . While these phase slips are more analogous to those observed in previous GaAs measurements [11], it is notable that the charge degeneracy line follows a nearly horizontal trajectory in the  $B$ - $V_P$  plane. This suggests a large capacitive lever arm between the plunger gate and the charge occupation number in the interferometer, at least for this particular charge trap. In fact, we find these strongly coupled charge loading events to be fairly ubiquitous in these devices. In the integer quantum Hall regime, where all phase slips are related to bulk-edge coupling effects, we find several isolated, reversible, slips where the slope of the charge degeneracy line varies depending on which gate is modulating the interference. We present here sample measurements of the interference on the inner edge of  $\nu = -2$ , where the slope of the charge degeneracy line is measured for various top-gate combinations. Taken collectively, the asymmetry in the lever arm of each top-gate to the charge trap occupation number, firmly indicates the charge trap is strongly localized. This further indicates that the disorder landscape in graphene van der Waals devices consists of sharp confining potentials, likely from Coulombic impurities in the hBN. This disorder picture, likely sufficiently different than in GaAs, will require new theoretical treatments of bulk edge coupling and how the spatial arrangement of charge affects future interferometry experiments.



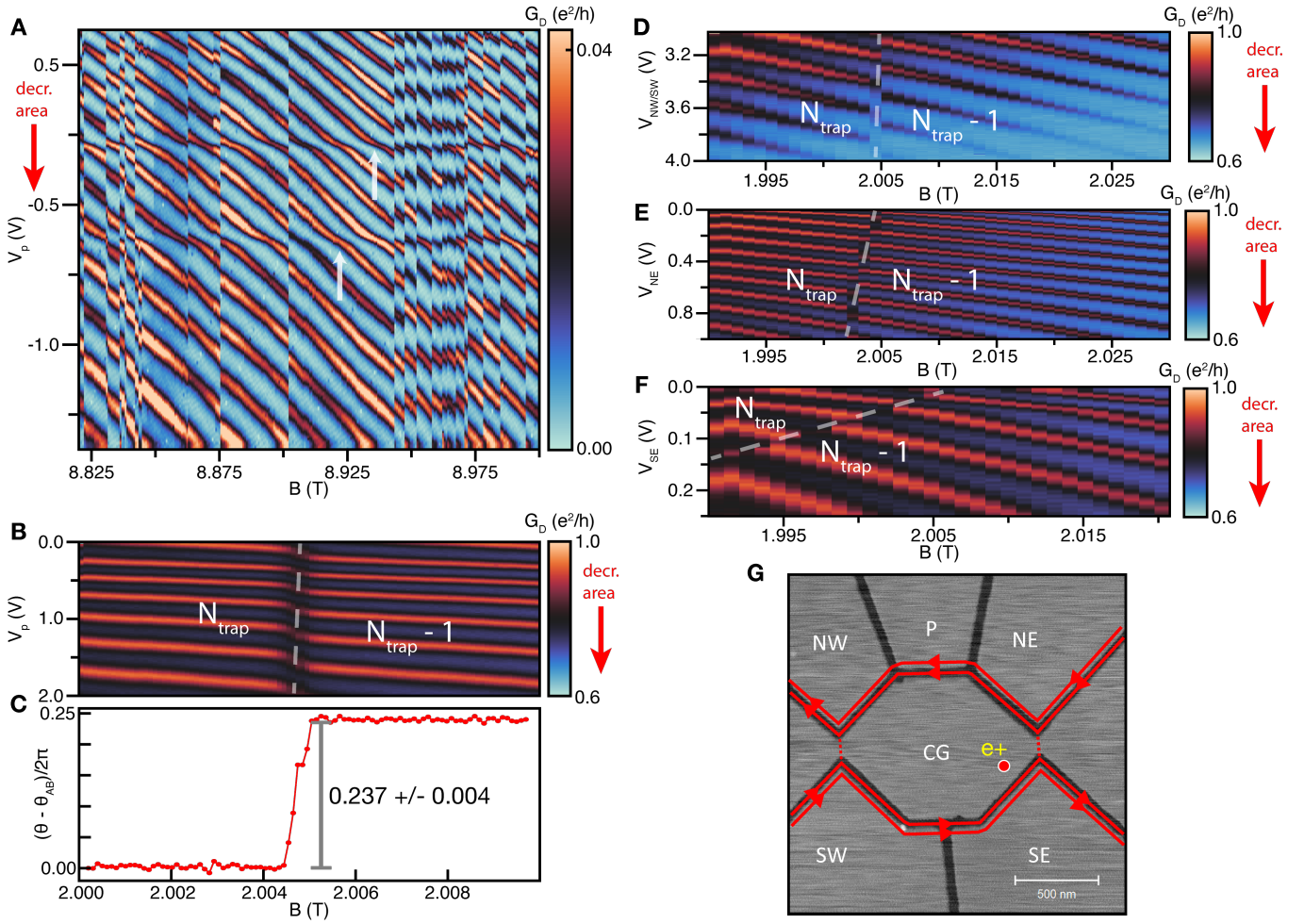


FIG. S11. **Soft-phase slips and locate-able defects.** (a) Full range of data explored for main text Fig. 1d. In addition to the sharp phase slips studied in the main text we also observe two distinct ‘soft’ phase slips that are continuously tuned by both  $V_P$  and  $B$  as indicated by the inset white arrows. We understand these to be sharp Coulombic defects that strongly localize charge near the edge. To validate this hypothesis we perform interference experiments in the integer quantum Hall regime, where no anyon phase effects should be expected, near one of these defects. (b) Isolated ‘soft’ phase slip across interference of the inner edge mode in  $\nu = -2$  in the second device shown in Fig. S1c-d.  $G_D$  is plotted versus  $V_P$  such that lines of constant Aharonov-Bohm phase have negative slope (plunger gate requires positive voltage to deplete the interferometer area on the hole side of the device). The phase slip is observed to have a nearly vertical slope in the  $B - V_P$  plane. The phase slip is the result of a finite amount of bulk-edge coupling when a single hole exits the interferometer. (c) Phase across the slip, with the Aharonov-Bohm component removed, calculated using the same DFT method used in the main text to extract the value of the sudden phase slips. (d)  $G_D$  as a function of  $B$  and  $V_{NW/SW}$  in the same operating regime as panel b, with all other gates fixed, which shows the same phase slip. Notably, the phase slip, similarly to panel b, has a nearly vertical slope in the  $B - V_{NW/SW}$  plane. (e)  $G_D$  as a function of  $B$  and  $V_{NE}$ , with all other gates fixed, again showing the same phase slip as in panel b. Here the phase slip is noted to have a steep, but discernibly less than vertical, slope in the  $B - V_{NE}$  plane. (f)  $G_D$  as a function of  $B$  and  $V_{SE}$ , all other gates fixed, showing the same phase slip as panel b. In this dataset the phase slip is shown to have an extremely shallow slope in the  $B - V_{SE}$  plane. This indicates a strong capacitive coupling to the charge trap not observed when studying the slip as the interference phase is varied using the other top gates. (g) AFM topograph, as shown in Fig. S1d, which shows the edge state configuration for panels b-f overlaid with the gate structure. The relative lever-arm each top gate has to the chemical potential of the charge trap allows us to put a strong constraint on the location of said trap. This location is marked by the red dot.

### S8. Anomalous State Preparation-Dependent Phase Slips

After the measurement presented in the main text Fig. 3 was performed, the center gate raster was continued over the trajectory shown in S12A. During the four subsequent sweeps up and down across the same range of  $V_C$ , no phase slips at all are observed, indicating that the system remains in a highly (meta)stable charge configuration. At 140 minutes, the  $V_C$  range was then made to excursion to a higher filling factor, before returning to the range studied previously (no interference is visible in this regime, as

the applied  $V_C$  causes the QPCs to be fully open). After this, the reverse-direction sweep to Fig. 3A was performed once again, and 11 phase slips were observed.

These phase slips present several mysteries. First, their magnitude is consistent, with an average value of  $\Delta\theta/2\pi = -0.425$  (See Fig. S12B). This is not particularly close to any integer multiple of  $2\pi/3$ , which suggests a significant and repeatable amount of bulk-edge coupling is relevant for every slip.

While their occurrence during an interval of decreasing of  $V_C$  leads one to expect they are associated with an overall removal of quasiparticles (addition of quasiholes), their magnitude is larger than  $-\theta_a$ . Due to the fact that bulk-edge coupling should only serve to decrease the magnitude of the phase slips, this leads one to the conclusion that each slip is associated with the removal of *more than one* quasiparticle every time. Confusingly, the magnitude of each slip is consistent, also suggesting that the *same number* of quasiparticles is removed with every event.

An alternative possibility to account for the consistent magnitudes would be that the system is merely switching back and forth between two distinct charge configurations. This should be considered, given that the phase slip magnitude is nearly  $\Delta\theta = \pm\pi$ , almost to within our expected systematic uncertainty. However, examination of the “charge fingerprint” of sets of curves which are separated by two phase slips (several of which are shown in Fig. S12D) indicates a strong degree of dissimilarity. This suggests that each charge configuration is in reality distinct.

While not definitive evidence, these facts taken together raise the possibility that after loading a higher density of quasiparticles, the unloading of these quasiparticles takes place in a correlated fashion, with each discretely-resolved event corresponding to the (at least nearly) simultaneous removal of more than one quasiparticle. This highlights the need for further experiments to probe the potentially complicated anyon dynamics in this system.

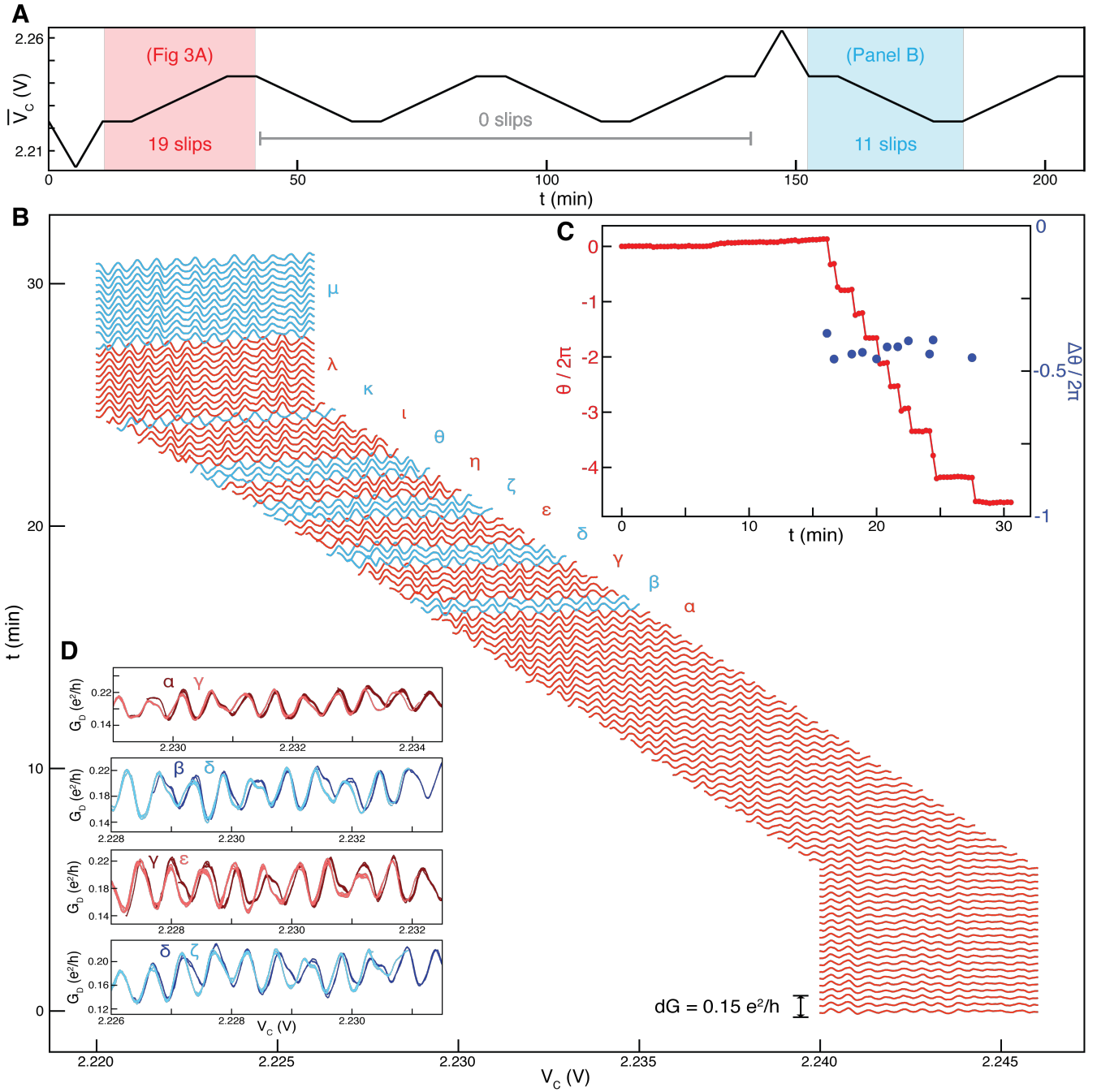


**FIG. S12. Anomalous phase jumps for a different state preparation.** (A) The trajectory of the center voltage of the  $V_C$  sweep. The data in main text Fig. 3A are taken from the indicated range. Subsequently 0 phase slips are seen as the gate voltage range is slowly swept back and forth over the same range. After an excursion to higher  $V_C$  at  $\sim 140$  min, the 11 slips analyzed here and shown in Panel B occur. (B) Analog of Fig. 4 in the main text, taken in the marked range of panel A, shortly after the gate voltage excursion to higher filling factor. (C) The extracted phase (in red) and magnitude of each discrete phase jump (in blue) of the data in panel B. (D) Overlapping traces from several classes that each are separated by two discrete jumps. The subtle differences in curve shape (“charge fingerprint”) indicate that, while the phase difference is nearly  $2\pi$ , the classes seem to correspond to distinct configurations of charge in the interferometer, ruling out that the observed phase slips are merely back-and-forth switching between two distinct charge states.

## S9. Additional data referenced in main text

Figure S13A-D show four repetitions of identically-measured interference data in the same regime as in the main text Fig. 1D. The exact locations of the individual phase slips differ between measurements. However, there is a clear increase in frequency of the slips in the high-field region of the plot (above 8.94 T). The extracted phase from each panel in Fig. S13E shows that in this range, while the exact location of the slips is random, their average spacing ensures that the phase remains roughly constant, with approximately one phase slip per additional flux quantum.

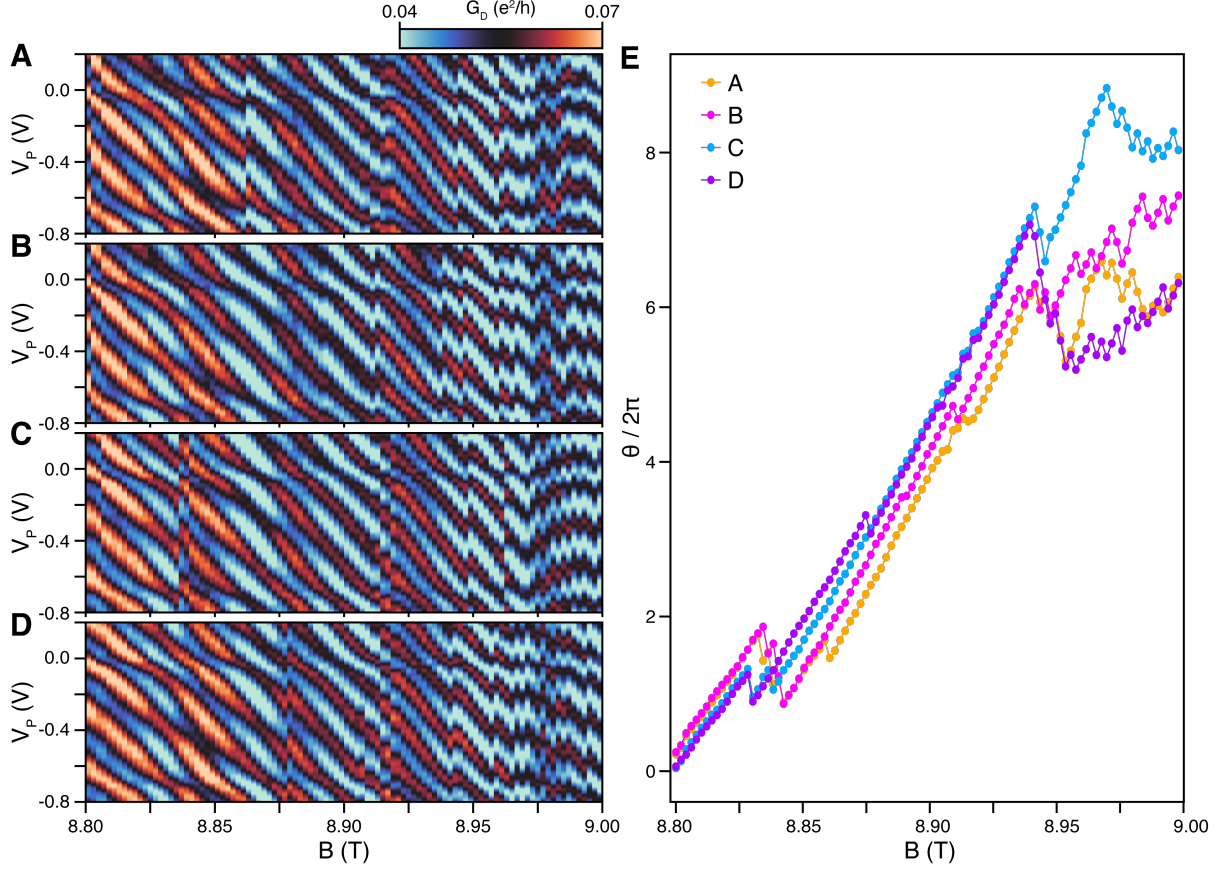


FIG. S13. **Repeated measurement of interference in the regime of Fig. 1** (A-D) Repeated measurements of  $G_D$  as a function of magnetic field and plunger gate voltage, corresponding to a subset of the range over which data in Fig. 1d were taken. The field is swept from low to high every time. (E) The extracted phase  $\theta$  as a function of  $B$ . No background is subtracted, but the line-by-line change in  $\theta$  is assumed to lie within the interval  $(-\pi, \pi)$ . The phase evolves smoothly due to the Aharonov-Bohm effect, and is punctuated by sharp slips corresponding to changes in the quasiparticle content. The spacing between these slips is stochastic, as the charging time is long — however, above 8.94T the slips happen approximately once per additional flux quantum, causing the phase to remain constant on average, despite large time-dependent deviations.

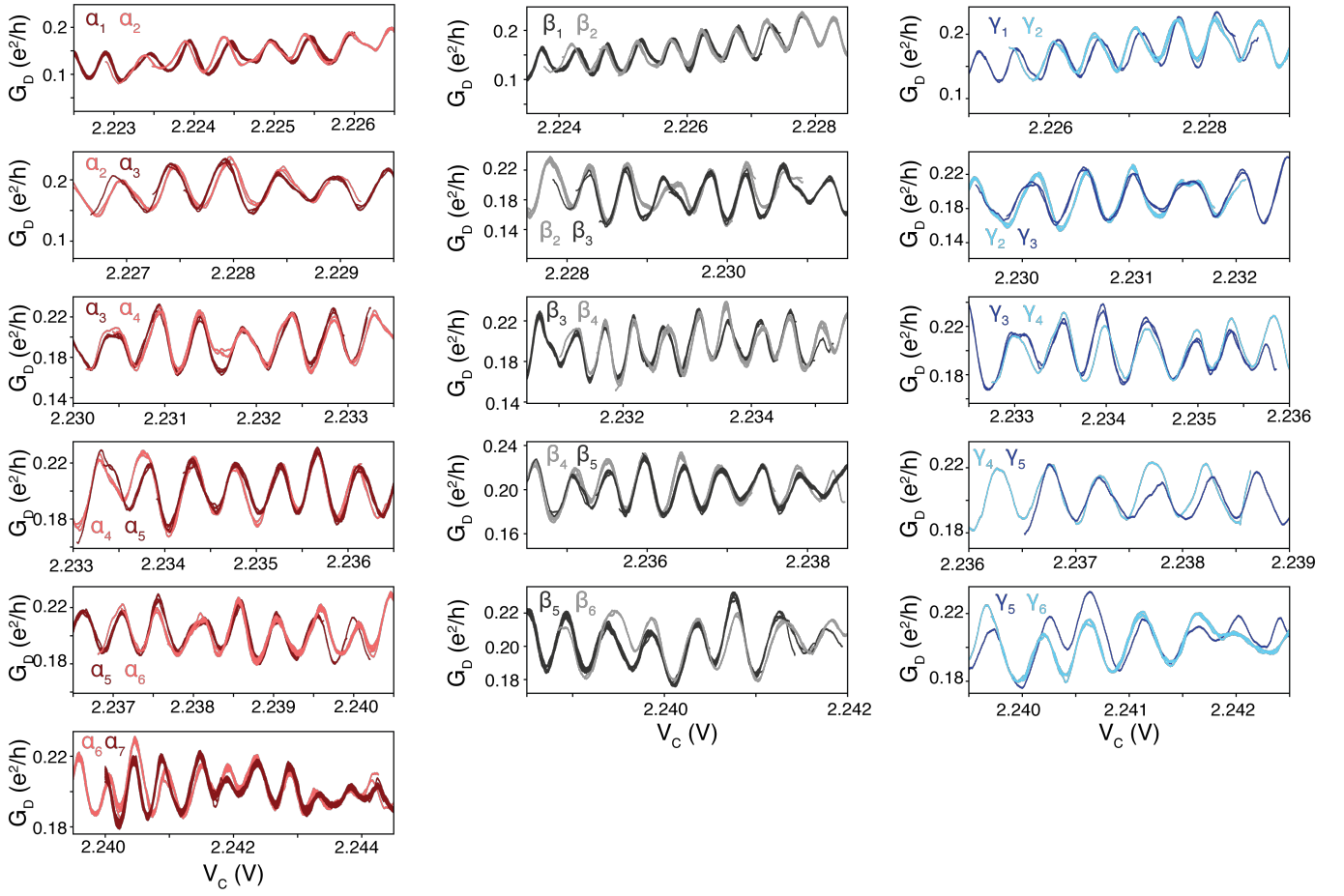


FIG. S14. Difference in charge fingerprint between all pairs of phase classes separated by 3 phase slips from Fig. 3 of the main text.

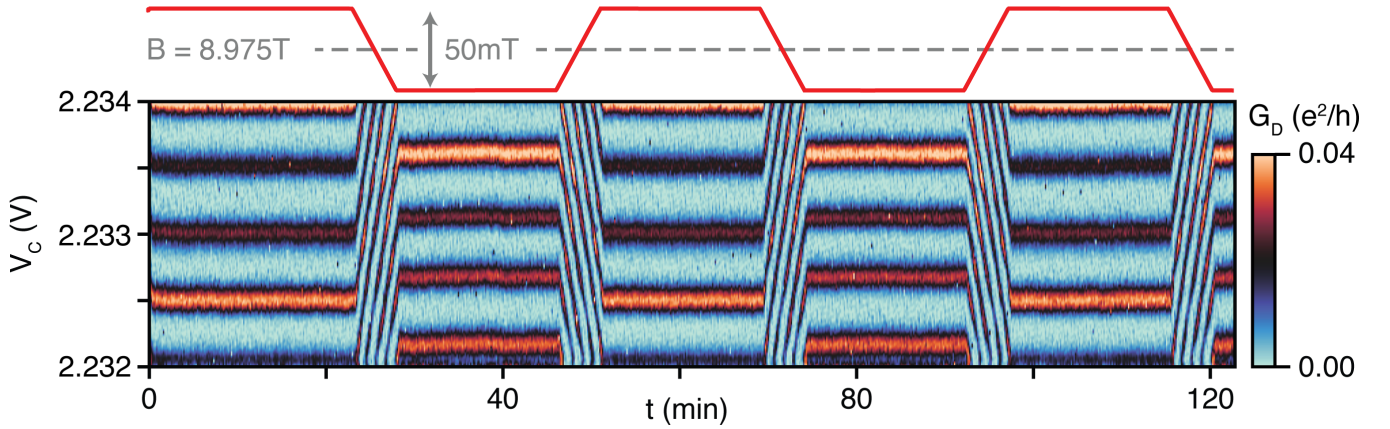


FIG. S15. Stability of phase over time while B field is swept. Repeated  $V_C$  ramps as a function of time, in a similar regime of parameters as those shown in Fig. 4. Here no phase slips are observed.